10-1994

Simulations of the Effects of Water Vapor, Cloud Liquid Water, and Ice on AMSU Moisture Channel Brightness Temperatures

Bradley M. Muller
Florida State University, mullerb@erau.edu

Henry E. Fuelberg
Florida State University

Xuwu Xiang
Florida State University

Scholarly Commons Citation

Muller, B. M., Fuelberg, H. E., & Xiang, X. (1994). Simulations of the Effects of Water Vapor, Cloud Liquid Water, and Ice on AMSU Moisture Channel Brightness Temperatures. *Journal of Applied Meteorology, 33*(10). https://doi.org/10.1175/1520-0450(1994)033<1133:SOTEOW>2.0.CO;2

Simulations of the Effects of Water Vapor, Cloud Liquid Water, and Ice on AMSU Moisture Channel Brightness Temperatures

BRADLEY M. MULLER,* HENRY E. FUELBERG, AND XUWU XIANG

Department of Meteorology, The Florida State University, Tallahassee, Florida

(Manuscript received 19 April 1993, in final form 15 January 1994)

ABSTRACT

Radiative transfer simulations are performed to determine how water vapor and nonprecipitating cloud liquid water and ice particles within typical midlatitude atmospheres affect brightness temperatures T_B's of moisture sounding channels used in the Advanced Microwave Sounding Unit (AMSU) and AMSU-like instruments. The purpose is to promote a general understanding of passive top-of-atmosphere T_B's for window frequencies at 23.8, 89.0, and 157.0 GHz, and water vapor frequencies at 176.31, 180.31, and 182.31 GHz by documenting specific examples. This is accomplished through detailed analyses of T_B's for idealized atmospheres, mostly representing temperate conditions over land. Cloud effects are considered in terms of five basic properties: droplet size distribution, phase, liquid or ice water content, altitude, and thickness. Effects on T_B of changing surface emissivity also are addressed. The brightness temperature contribution functions are presented as an aid to physically interpreting AMSU T_B's.

Both liquid and ice clouds impact the T_B's in a variety of ways. The T_B's at 23.8 and 89 GHz are more strongly affected by altostratus liquid clouds than by cirrus clouds for equivalent water paths. In contrast, channels near 157 and 183 GHz are more strongly affected by ice clouds. Higher clouds have a greater impact on 157- and 183-GHz T_B's than do lower clouds. Clouds depress T_B's of the higher-frequency channels by suppressing, but not necessarily obscuring, radiance contributions from below. Thus, T_B's are less closely associated with cloud-top temperatures than are IR radiometric temperatures. Water vapor alone accounts for up to 89% of the total attenuation by a midtropospheric liquid cloud for channels near 183 GHz. The Rayleigh approximation is found to be adequate for typical droplet size distributions; however, Mie scattering effects from *liquid* droplets become important for droplet size distribution functions with modal radii greater than 20 μm near 157 and 183 GHz, and greater than 30–40 μm at 89 GHz. This is due mainly to the relatively small concentrations of droplets much larger than the mode radius. Orographic clouds and tropical cumuli have been observed to contain droplet size distributions with mode radii in the 30–40-μm range. Thus, as new instruments bridge the gap between microwave and infrared to frequencies even higher than 183 GHz, radiative transfer modelers are cautioned to explicitly address scattering characteristics of such clouds.

1. Introduction

New generations of polar-orbiting weather satellites to be launched in the 1990s will have improved capabilities for sensing moisture in both vapor and condensed forms. With channels near 89, 157, and 183 GHz, these satellites will achieve higher vertical and horizontal resolution than the current Microwave Sounding Unit (MSU) and will be less sensitive to clouds than infrared (IR) sensors. The new Advanced Microwave Sounding Unit (AMSU) will provide operational weather information from the NOAA-K, NOAA-L, and NOAA-M satellites and also research data as an instrument for NASA's Earth Observing System (EOS). AMSU consists of two components: AMSU-A includes temperature sounding channels and two moisture channels at 23.8 and 89 GHz with nadir resolution of 50 km. AMSU-B contains moisture sounding channels at 89, 150, 183.31 ± 7.0, 183.31 ± 3.0, and 183.31 ± 1.0 GHz with nadir resolution of 15 km. Additionally, the Defense Meteorological Satellite Program's (DMSP) SSM/T-2 [Special Sensor Microwave Water Vapor Sounder, Griffin et al. (1993); Boucher et al. (1993)] instrument, launched in November 1991, contains frequencies similar to AMSU-B, as will the MHS [Microwave Humidity Sounder, Saunders (1993)], and the DMSP's future SSMIS [Special Sensor Microwave Imager/Sounder, Swadley and Chandler (1992)]. There also are plans for microwave (MW) sounders to be carried on future geostationary platforms.

While AMSU data will provide operational temperature and moisture profiles for use in numerical

* Current affiliation: Center for Clouds, Chemistry and Climate, Scripps Institution of Oceanography, University of California, San Diego, La Jolla, California.

Corresponding author address: Bradley M. Muller, Center for Clouds, Chemistry and Climate, SIO/UCSD-Mail Code 0239, La Jolla, CA 92093-0239.

weather prediction, some channels will yield imagery similar to those of current IR window and water vapor channels. For example, 89 GHz is a window frequency that can be considered an MW analog to the 11-μm IR window channel. An important difference is that the MW channel can partially penetrate clouds; thus, aircraft measurements at 92 GHz have correlated with radar echoes from the upper portions of convective storms (Hakkarinen and Adler 1988; Heymsfield and Fulton 1988). Mugnai et al. (1993) give a detailed discussion of the microphysical constituents and source layers directly sensed by multifrequency passive MW observations. The 183-GHz channels are located in a strong water vapor absorption line and are MW analogs to IR channels in the 6.3-μm water vapor vibration–rotation band. Imagery from frequencies sensitive to middle- and upper-tropospheric water vapor produces brightness temperature T_B signatures associated with kinematic, dynamic, and thermodynamic atmospheric processes (e.g., Petersen et al. 1984; Uccellini et al. 1985; Muller and Fuelberg 1990; Weldon and Holmes 1991).

The role of clouds in MW remote sensing problems has been the subject of discussion in recent years. For example, Wilheit (1986) suggested that cloud liquid water is a relatively benign component of the MW precipitation retrieval problem. However, Mugnai and Smith (1984), Mugnai and Smith (1988), Mugnai et al. (1990), and Adler et al. (1991) have shown that cloud liquid water significantly affects MW T_B's. At the so-called millimeter-wave frequencies of 89, 157, and 183 GHz, T_B effects from cloud liquid water can be substantial (Isaacs and Deblonde 1987; Wilheit 1990; Muller et al. 1992; Huang and Diak 1992). Additionally, a crucial question regarding these high-frequency MW channels is how their measurements respond to cirrus ice clouds (e.g., Eyre 1990; Wilheit 1990).

Much of the previous research on MW moisture channels has focused on water vapor profiling. Wang et al. (1989) noted that channels near the weak water vapor line at 22.2 GHz provide only enough sensitivity to measure total column (precipitable) water vapor and cannot be used over land where the high emissivity obscures the atmospheric contribution. They do have the advantage of being relatively insensitive to nonprecipitating clouds. The 183-GHz channels first were investigated using radiative transfer simulations for clear-sky water vapor profiling (Schaerer and Wilheit 1979; Rozenkranz et al. 1982; Kakar 1983; Kakar and Lambrigtsen 1984; Wang et al. 1983). More recent simulations have begun to include the effects of cloud liquid water on retrievals (Isaacs and Deblonde 1987; Eyre 1990; Wilheit 1990; Wang et al. 1989; Wang and Chang 1990; Diak et al. 1992). For example, Wilheit pointed out that clouds themselves can provide water vapor information for retrievals. However, these studies have not examined Mie scattering from large liquid cloud droplets or effects of cloud ice. The present research addresses these issues and attempts to separate the contributions of cloud water and water vapor within cloud layers to upwelling T_B's.

The literature contains few studies about the impact of nonprecipitating cloud ice on millimeter-wavelength channels. Aircraft observations of thunderstorms indicate that the 92- and 183-GHz frequencies are significantly less sensitive to anvil cirrus than are corresponding IR measurements (Hakkarinen and Adler 1988; Heymsfield and Fulton 1988). Thus, many previous modeling experiments have concentrated on the effects of precipitation-sized liquid and ice particles (e.g., Wilheit et al. 1982; Wu and Weinman 1984; Yeh et al. 1990). Nevertheless, spherical cirrus ice particles with radii ranging from 50 to 1000 μm reduced T_B's through scattering in simulations of the 118-GHz oxygen channel (Weinman 1988). More recently, Muller et al. (1993) used spherical particles to demonstrate the importance of accounting for very high concentrations of cirrus-sized ice in T_B simulations near 90 and 183 GHz over a thunderstorm. Smith et al. (1992) discussed spherical ice crystal parameterization for calculating T_B's at MW frequencies up to 128 GHz over a precipitating model thunderstorm. The shape of ice particles also affects T_B's (Evans and Vivekanandan 1990). They found that hexagonal plate sizes from 60 to 2000 μm produced simulated 157-GHz T_B's that deviated from the equivalent spherical approximation by up to 15°C.

The goal of our research is to explore the use of AMSU imagery for interpreting dynamic, kinematic, and synoptic properties of the atmosphere. This requires a thorough understanding of the physical processes that lead to upwelling T_B's, as well as the typical ranges and sensitivities of those T_B's to atmospheric constituents. The purpose of this paper is to promote a general understanding about the effects of water vapor, and liquid and ice clouds on T_B's from AMSU and AMSU-like moisture sounding channels by documenting specific examples. We employ a conceptually simple framework using idealized cloud, temperature, and water vapor profiles as input to a Sobolev radiative transfer model (Xiang 1989) to produce T_B simulations for nonprecipitating atmospheres. The examples focus mainly on temperate midlatitude atmospheres over land, but include a few cases over water. The frequencies being examined are 23.8, 89, 157, 176.31, 180.31, and 182.31 GHz. After our simulations were completed, 150 instead of 157 GHz was established as the AMSU-B channel to be employed on the first few launches, while 157 will be used on the MHS. However, this minor difference in frequencies does not substantially affect the basic concepts discussed in this paper. Precipitation signatures for T_B's near 89 and 183 GHz have been addressed elsewhere (e.g., Wilheit et al. 1982; Heymsfield and Fulton 1988; Fulton and Heymsfield 1991; Hakkarinen and Adler 1988; Adler et al. 1990;

Adler and Hakkarinen 1991; Yeh et al. 1990; Muller et al. 1993) and are not considered here.

The paper is presented in five major sections. Theoretical considerations pertaining to the physical interpretation of AMSU moisture channel T_B's are presented in section 2. Methodology about the radiative transfer model, cloud models, and idealized atmospheric profiles is described in section 3. Section 4 gives results of T_B simulations for both clear and cloudy atmospheres. Conclusions are presented in section 5.

2. Radiative transfer considerations

Upwelling top-of-atmosphere (TOA) T_B's result from a complex combination of radiative interactions with atmospheric constituents and the earth's surface. Important atmospheric radiative processes in the MW spectrum include gaseous absorption and emission, and absorption, emission, and scattering from both liquid and frozen hydrometeors. Important surface radiative processes include absorption, emission, and reflection. Contribution functions (CFs) quantitatively describe these processes and thus are useful for analyzing the TOA T_B. They represent the proportion of radiation per kilometer of vertical atmosphere that each layer contributes to the total T_B and the fraction contributed by the surface. The CF formulation employed here follows from the radiative transfer equation. It is analogous to Smith and Mugnai's (1989) and Mugnai et al.'s (1993) "generalized weighting function" but is calculated in terms of radiance (intensity) rather than irradiance (flux).

The radiative transfer equation for a plane-parallel atmosphere is

$$\mu \frac{dI}{d\tau} = I - J, \tag{1}$$

where I is the radiance, τ is the cumulative optical depth increasing from the TOA downward, μ is the cosine of the zenith angle defined as a positive quantity throughout this paper, and J is the source function incorporating emission and scattering. With the assumption of azimuthal independence, and with I expressed in terms of brightness temperature, J is given by

$$J(\tau, \mu) = \frac{\omega(\tau)}{2} \int_{-1}^{1} P(\tau; \mu, \mu') I(\tau, \mu') d\mu' + [1 - \omega(\tau)] T(\tau), \tag{2}$$

where ω, P, and T are the single-scatter albedo, the average scattering phase function for an ensemble of particles, and the environmental temperature, all at τ. The phase function $P(\tau; \mu, \mu')$ describes the average contribution from radiation incident on particles at arbitrary zenith angle μ' that is scattered into the observation zenith angle μ. Thus, the first term of (2) quantifies the scattering source, while the second term describes the source due to atmospheric emission.

A solution to (1) for upwelling radiation incorporating the boundary condition for a Lambertian surface is

$$I(0, \mu) = [(1 - \epsilon_S)\bar{I}\downarrow + \epsilon_S T_S] \exp\left(-\frac{\tau_S}{\mu}\right) + \int_0^{\tau_S} J(\tau', \mu) \exp\left(-\frac{\tau'}{\mu}\right) \frac{d\tau'}{\mu}, \tag{3}$$

where $\bar{I}\downarrow$ is the average downwelling radiance at the surface expressed in terms of brightness temperature, T_S is the surface skin temperature, ϵ_S is the surface emissivity, and τ_S is the optical depth of the entire atmosphere.

Smith and Mugnai (1989) showed that the contribution to the upwelling intensity C_I from a thin layer of optical depth $\delta\tau$ at altitude z to radiance at the "top" of the atmosphere, $z = z_T$, is

$$C_I(z, \mu) = \frac{\delta\tau}{\mu} J(z, \mu) \exp\left[\frac{-\tau(z)}{\mu}\right], \tag{4}$$

where $\tau(z)$ represents the optical depth between the source level z and z_T, and

$$\tau(z) = \int_z^{z_T} \beta_{\text{ext}}(z') dz', \tag{5}$$

where β_{ext} is the volume extinction coefficient. Equation (4) essentially represents the integrand of (3) (Wu and Weinman 1984). Physically, it expresses the radiative sources from an atmospheric layer at height z, attenuated by the transmittance, $\exp(-\tau/\mu)$. In practice, the integral in (3) is separated into individual integrals for each atmospheric layer, which then are evaluated using an analytic form of the source function derived in the Sobolev solution to the radiative transfer equation. For a Lambertian surface, the surface contribution to the upwelling intensity C_S is given by the first term of (3):

$$C_S = [(1 - \epsilon_S)\bar{I}\downarrow + \epsilon_S T_S] \exp\left(\frac{-\tau_S}{\mu}\right). \tag{6}$$

The first term on the right represents surface reflection of downwelling radiation, while the second term denotes surface emission. The transmittance factor $\exp(-\tau_S/\mu)$ attenuates the surface emission and reflection through cumulative extinction by the optical depth. The sum of the contributions from all thin layers of optical depth plus the surface contribution is the TOA T_B that would be measured by a satellite:

$$T_B = \sum_{i=1}^{N} C_I(z_i, \mu) + C_S, \tag{7}$$

where N is the number of layers in the discretized model atmosphere. To obtain the contribution functions, we

simply calculate the fractional contributions by dividing the C_I's for each layer by the TOA T_B and then normalize by the vertical thickness of the emitting layer to obtain units of inverse kilometers:

$$\mathrm{CF}(z_i, \mu) = \frac{C_I(z_i, \mu)}{T_B \delta z_i}. \quad (8)$$

Similarly, the fractional surface contribution is

$$\mathrm{CF}(z = 0, \mu) = \frac{C_S}{T_B}. \quad (9)$$

Like Mugnai et al.'s (1993) generalized weighting function, the CF is normalized such that integrating it with respect to height and adding the fractional surface contribution yields a value of 1.0. In contrast to traditional clear-air weighting or contribution functions of well-mixed gases such as CO_2 and O_2, the vertical structure of our CFs is highly variable due to the concentrations and altitudes of water vapor, precipitation, and cloud liquid and ice particles (i.e., those constituents that compose the optical depth). Equations (4) and (6) along with (2) indicate that TOA T_B's are determined by the temperature and emissivity of the emitting medium, the scattering source, and the attenuation of these contributions by the intervening optical depth between the sensor and sources. Attenuation (extinction) can occur through absorption or scattering.

The electromagnetic spectrum for the MW region (e.g., Ulaby et al. 1981) determines the radiative and gaseous interactions for the AMSU moisture channels. The main atmospheric absorbing gases are water vapor and oxygen. Since the 23.8-GHz AMSU channel is located on the wings of a weak water vapor absorption line, radiation absorption by water vapor is relatively small. The 89-GHz channel exhibits slightly greater water vapor absorption due to the continuum, but in a clear atmosphere, surface contributions dominate both channels. This is very important for interpreting T_B's, because surface emissivity in the MW region is highly variable. On the other hand, the proximity of AMSU's three 183-GHz channels to the center of the 183.31-GHz water vapor absorption line determines their response to the vapor. Each AMSU channel in this portion of the spectrum exploits the relative symmetry of the line by measuring in bands on both sides to improve its signal-to-noise ratio. In clear conditions, the 183.31 ± 3.0- and 183.31 ± 7.0-GHz frequencies respond mostly to absorption and emission by lower- and midtropospheric water vapor where pressure broadening makes contributions from the wings relatively strong. Conversely, the 183.31 ± 1.0-GHz frequency measures radiation near the line core and thus is sensitive to even the small amounts of water vapor in the middle and upper troposphere. These effects strongly differentiate T_B's of the three channels in clear air. We will refer to frequencies near 183 GHz as "water vapor" channels, while those at 23.8 and 89 GHz will be termed "window" channels.

Satellite-derived radiation measurements at the TOA are influenced by a number of fundamental cloud properties: altitude, vertical depth, and microphysical characteristics such as phase, liquid or ice content, and particle size, shape, and density. These microphysical parameters determine the optical properties for ensembles of cloud particles. In terms of spherical particles, the ratio of the radius r to the radiation's wavelength λ, known as the size parameter x, is given by

$$x = 2\pi \frac{r}{\lambda}. \quad (10)$$

If we adopt $x = 0.1$ as the cutoff separating Rayleigh particles from those where Mie scattering becomes important (e.g., Wallace and Hobbs 1977), the full Mie solution is required for sizes greater than approximately 200 μm at 23.8 GHz, and above 60 μm at 89 GHz. The cutoff for 157.0 GHz is approximately 40 μm, while for the three 183-GHz channels it is approximately 30 μm. For a radius of 40 μm, the difference in x between 176.31 and 182.31 GHz is only about 3%. This means that all three 183-GHz channels respond nearly equally to hydrometeors. However, contrasting gaseous absorption tends to differentiate T_B's of the three channels. Section 4 uses radiative theory to explain how specific atmospheric profiles result in TOA T_B's.

3. Methodology

a. Radiative transfer models

Our radiative transfer model is based on Xiang's (1989) multilayer Sobolev solution to the radiative transfer equation. It is a plane-parallel two-stream multiple scattering solution for T_B that is comparable to an Eddington model (e.g., Wu and Weinman 1984). It has shown good accuracy when compared to multistream models. An unpolarized version having 76 vertical layers at a resolution of 0.25 km and viewing at nadir has been employed here. Optical parameters for polydisperse size distributions of spherical liquid and frozen hydrometeors were calculated for each layer using Wiscombe's (1980) Mie algorithm and are considered constant across the entire layer. Complex refractive indices of water were calculated according to Ray (1972), while those of ice used the algorithms of Warren (1984). For computational efficiency, look-up tables of the optical parameters were constructed based on temperature and liquid or ice water content (LWC or IWC). Gaseous absorption for each layer was calculated from idealized soundings using an updated version of Liebe's (1985) algorithm.

The solution (3) to the radiative transfer equation is evaluated in the following manner. Under the Sobolev approach, the radiance is expanded in terms of the cosine of the azimuth angle. Manipulation yields linear equa-

tions for the mean diffuse radiance and flux for each layer. Coefficients are derived through simultaneous solution after applying boundary conditions at the top and bottom of the atmosphere and requiring equality at the layer interfaces. Using the coefficients, the source function for each layer can be expressed as an analytical function of optical depth and the optical constants. The source functions can then be integrated analytically. For a multilayer atmosphere, the upwelling radiation calculation begins with the surface boundary condition, then steps upward recursively, computing the radiance at the top of each new layer using the upward radiance from the last layer as the bottom boundary condition.

Several simplifications shaped our radiative transfer approach. All hydrometeors were assumed spherical, homogeneous, and either liquid or frozen. The density of frozen particles was set at 0.917 g cm^{-3}. The calculations were performed monochromatically at nadir-viewing angle for frequencies representing each AMSU moisture channel. For computational efficiency, only one side of the two-sided 183-GHz channels was calculated (e.g., Kakar 1983). The Rayleigh–Jeans approximation to the Planck function was applied so that upwelling radiance was calculated directly in terms of T_B. Since the atmosphere was assumed plane parallel for each sounding, the calculated T_B's represent conditions everywhere within a satellite footprint. Thus, as with Isaacs and Deblonde (1987), these calculations may represent an upper bound for the impacts of stratified clouds. The nadir-viewing and spherical particle framework eliminate the need to consider polarization.

A final simplification was the use for all frequencies of a constant surface emissivity of 0.9 to represent land and, following Isaacs and Deblonde (1987), 0.7 to represent the ocean. Oceanic emissivity is variable across frequency and also depends strongly on the physical condition of the surface. Previous work (e.g., Wilheit 1978; Grody 1988) suggests that nadir-viewing sea surface emissivity could be as low as 0.4 for lower-frequency channels such as 23.8 GHz and are near 0.6 at 89 GHz. Very little has been published regarding surface emissivity near 157 and 183 GHz. Calculations using the model of Klein and Swift (1977) indicate that 0.7 is an appropriate nadir-viewing value at these frequencies (Grody 1993, personal communication). Recent retrievals by Felde and Pickle (1994) from SSM/T-2 data at 91 and 150 GHz over water showed mean values near 0.6 for unsaturated atmospheric profiles with a variety of viewing angles. While differences in surface emissivity can have a large effect on window channel T_B's (e.g., T_B at 23.8 GHz increases by approximately 20 K as ϵ_S increases by 0.1), the use of a generic value of 0.7 for all frequencies serves to qualitatively illustrate the effects of reducing surface emissivity from land values. In general, using lower values of ϵ_S for calculations accentuates effects related to surface reflection such as those described in section 4b.1.

b. Atmospheric profile and cloud models

Experiments were performed using both clear and cloudy atmospheric profiles. All temperature profiles employed the U.S. standard atmospheric lapse rate of 6.5°C km^{-1}. Surface temperature (and consequently all temperatures above) were adjusted according to the needs of the particular experiment. Moisture profiles generally were defined by a constant background tropospheric dewpoint depression T_{dd}, with specific moist layers superimposed in some cases. The atmosphere within a cloud layer was specified to be saturated; that is, T_{dd} was set to zero. Above the tropopause, the dewpoint temperature T_d decreased linearly to a constant value of −80°C.

Droplet size distribution functions (SDFs) for water clouds were calculated using the modified gamma function (Deirmendjian 1969; Tampieri and Tomasi 1976; Falcone et al. 1979; Welch et al. 1980; Smith et al. 1992; Muller et al. 1993). The modified gamma function yields a generic family of curves whose parameters can be fit to actual particle distributions. Integrating the particle SDF and volume formula with respect to radius gives LWC or IWC. A given size distribution can be scaled to a desired LWC by multiplying the droplet number concentration in each radius category by the ratio of the desired LWC to the original LWC. The modified gamma parameters used here described altostratus clouds having a mode radius (radius of maximum particle frequency) of 4.5 μm (Falcone et al. 1979; Isaacs and Deblonde 1987).

Cirrus clouds were specified by Starr and Cox's (1985) bimodal version of the modified gamma function that represents a large particle mode superimposed on a small particle mode, very similar to observations of cirrus uncinus by Heymsfield (1975). The Starr and Cox formulation gives crystal lengths rather than spherical radii. Therefore, despite shortcomings of the spherical approximation, we transformed their SDFs to spherical radii of equivalent mass using their exponential formulas for particle mass as a function of crystal length. We employed their parameters for cirrus uncinus with small and large particle mode lengths of 10 and 500 μm, respectively, retained their equipartition between bullet rosette and column crystal habits, and assumed an ice density of 0.917 g cm^{-3}. This yielded SDFs for equivalent spherical particles with mode radii of approximately 2 and 110 μm for the small and large crystal modes, respectively. Since much of the ice mass is concentrated in the small particle mode of the bimodal distribution, we expect T_B's to be affected somewhat less by the spherical assumption than the calculations by Evans and Vivekanandan (1990).

4. Results

This section describes the influence of atmospheric temperature, water vapor, liquid and ice clouds, and surface emissivity on AMSU moisture channel T_B's.

The experiments on clouds examine T_B's in terms of five basic cloud properties: droplet size distribution, phase, liquid or ice content, altitude, and vertical thickness.

a. Clear atmospheres

AMSU moisture channels detect water vapor over a range of altitudes in the troposphere. As an example, Fig. 1a shows CFs, fractional surface contributions, and TOA T_B's for an atmosphere having a 1000-mb temperature of 25°C, a lapse rate of 6.5°C km^{-1}, and the uniform T_{dd} of 15°C (solid lines in Fig. 1d). We have labeled channels 1–6 in the diagrams in order of increasing altitude of maximum sensitivity and frequency, that is, 23.8, 89.0, 157.0, 176.31, 180.31, and 182.31 GHz, respectively. Hereafter, the channels are referred to by their approximate modeled frequencies (e.g., "channel 176"). Figure 1a shows that channels 23.8, 89, and 157 all have strong surface contributions, while channel 176 peaks near 790 mb and channels 180 and 182 peak near 590 and 440 mb, respectively. Other aspects of Fig. 1 will be discussed in section 4b.

It is informative to examine how variations in water vapor, temperature, and surface emissivity affect T_B's from the AMSU moisture channels. Simulated T_B's

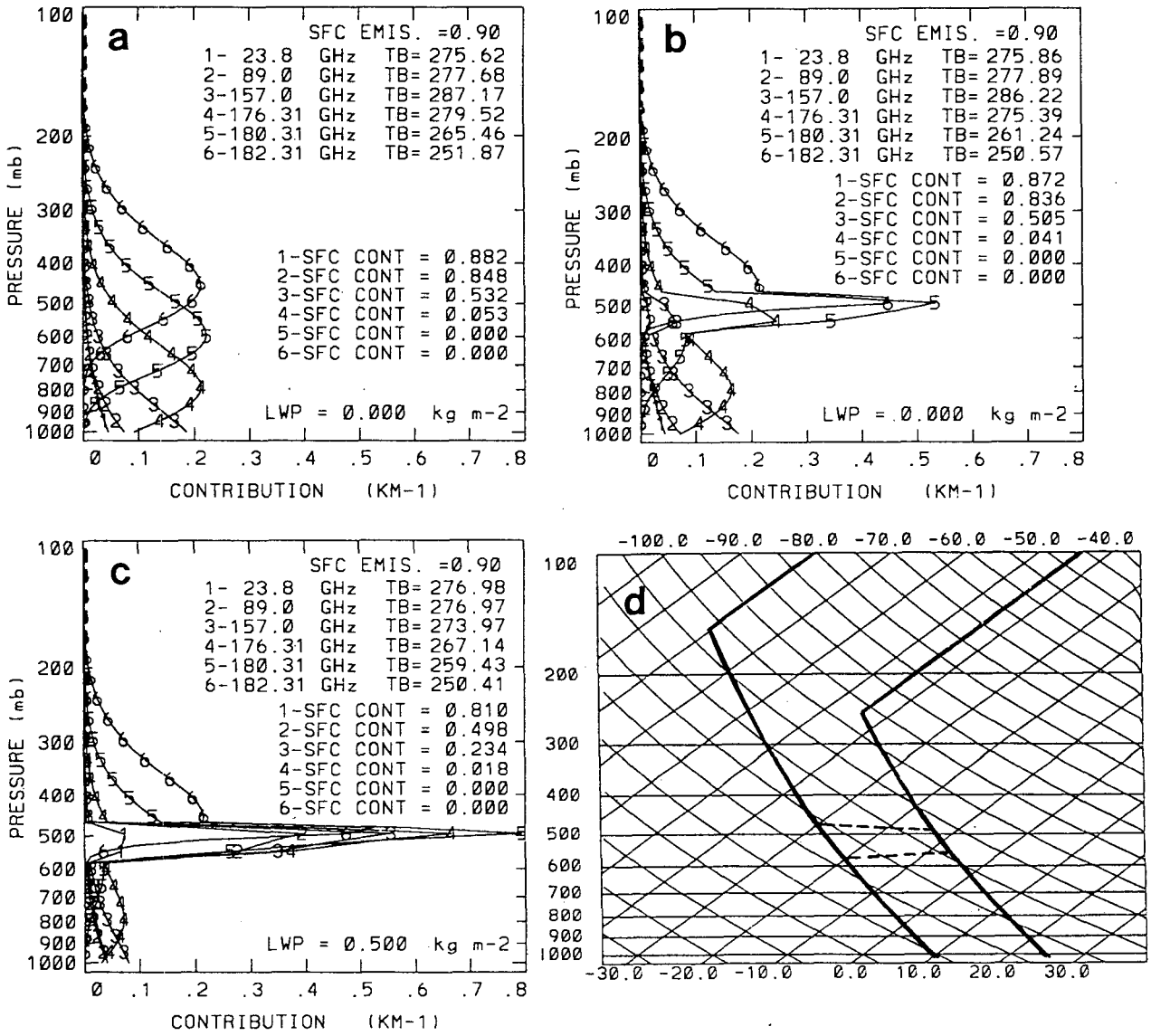

FIG. 1. Contribution functions (km^{-1}) for six AMSU moisture channels for (a) uniform T_{dd} profile; (b) as in (a) but with a single moist layer; (c) as in (b) but with 0.4 g m^{-3} liquid cloud water in the moist layer; and (d) skew T–log$p$ plot of atmospheric temperature and dewpoint (°C) profiles corresponding to (a), (b), and (c); dashed line indicates moist layer. The T_B's and fractional surface contributions for each channel are given on the right portions of (a)–(c).

for eight different clear atmospheric soundings are provided in Table 1. The table also includes percentages of surface T_B contributions and the pressure levels of CF peaks. Table 2 describes characteristics of the idealized soundings. All employ the U.S. standard atmospheric lapse rate of 6.5°C km^{-1}. The T_B effects due solely to water vapor can be investigated by changing the dewpoint profile while holding the temperature constant. Sounding 1 represents a very moist July sounding with a 1000-mb temperature of 30°C and a tropospheric T_{dd} of 5°C, while sounding 2 contains the same temperature structure but is much drier (a tropospheric T_{dd} of 20°C). Both use a "land" surface emissivity value of 0.9. Decreasing the tropospheric water vapor content allows the water vapor channels to see the lower, warmer portions of the atmosphere. For example, CF peaks for channels 176, 180, and 182 of sounding 1 are 610, 450, and 330 mb, respectively. However, they move to 790, 600, and 460 mb for the drier sounding 2. This agrees qualitatively with results of Schaerer and Wilheit (1979) and Wang et al. (1983). The greater contributions from the lower, warmer layers increase T_B's for channels 176, 180, and 182 by approximately 15 K (to 285, 271, and 256 K, respectively).

The T_B's for channels 23.8 and 89 experience the opposite trend, decreasing by 6 and 9 K (to 280 and 282 K) for the drier profile. This response is due to the changing contrast between emission from the relatively warm lower troposphere and the radiometrically cool surface background emission given by the product of ϵ_S (0.9) and T_S (303.15 K) as 272.8 K. That is, as the profile dries, emission from warm atmospheric water vapor in the lower layers decreases, and the TOA T_B cools toward that of the surface emission. For large values of surface emissivity, $\epsilon_S T_S$ is the dominant term of (6). In summary, while MW water vapor channel T_B's (i.e., those near 183 GHz) generally are warmed because drying enables them to "see" to lower, warmer atmospheric layers, T_B's of the MW window channels (23.8 and 89 GHz) are cooled because drying exposes more of the radiometrically cool surface contribution.

In agreement with Kakar and Lambrigtsen (1984), decreasing the surface emissivity from the land value enhances the influence of water vapor on T_B's in some channels. Soundings 3 and 4 are the same as 1 and 2, but employ a surface emissivity of 0.7 to simulate the ocean. In this case, the surface emission ($\epsilon_S T_S = 212.2$ K) is radiometrically colder than emission from the lower atmosphere, causing channels 23.8 and 89 to be more sensitive to water vapor changes in the lower levels. For example, T_B's for channel 89 decrease by 34 K from sounding 3 to 4, compared with only a 9-K decrease from sounding 1 to 2. This again is due to

TABLE 1. Clear-air brightness temperatures, surface contributions, and CF peaks for eight soundings at AMSU moisture channel frequencies.

	Sounding number							
Channel	1	2	3	4	5	6	7	8
1—23.8 GHz								
T_B (K)	286.27	280.06	260.68	236.48	281.96	248.34	243.50	198.72
Sfc. contribution (%)	72.6	88.5	69.9	86.3	84.4	96.7	81.9	95.8
CF peak (mb)	sfc	sfc	sfc	sfc	sfc	sfc	sfc	sfc
2—89.0 GHz								
T_B (K)	290.78	281.82	276.07	241.68	284.70	248.62	251.94	199.28
Sfc. contribution (%)	59.2	85.7	57.0	83.4	79.5	96.4	76.8	95.6
CF peak (mb)	sfc	sfc	sfc	sfc	sfc	sfc	sfc	sfc
3—157.0 GHz								
T_B (K)	287.89	291.67	287.55	279.34	292.57	252.36	286.91	212.03
Sfc. contribution (%)	13.5	55.5	13.4	53.5	41.6	89.3	40.4	87.3
CF peak (mb)	860	sfc	sfc	sfc	sfc	sfc	sfc	sfc
4—176.31 GHz								
T_B (K)	270.87	284.95	270.87	284.89	280.38	262.16	280.37	248.38
Sfc. contribution (%)	0.0	6.3	0.0	6.3	1.8	60.1	1.7	57.8
CF peak (mb)	610	790	610	790	720	sfc	720	sfc
5—180.31 GHz								
T_B (K)	255.91	270.66	255.91	270.66	265.70	261.34	265.70	260.27
Sfc. contribution (%)	0.0	0.0	0.0	0.0	0.0	22.7	0.0	22.4
CF peak (mb)	450	600	450	600	540	900	540	900
6—182.31 GHz								
T_B (K)	239.62	255.57	239.62	255.57	250.17	251.88	250.17	251.82
Sfc. contribution (%)	0.0	0.0	0.0	0.0	0.0	5.7	0.0	5.7
CF peak (mb)	330	460	330	460	410	730	410	730

TABLE 2. Characteristics for soundings used to create Table 1.

Sounding	1000-mb temperature (°C)	Tropospheric T_{dd} (°C)	Surface emissivity	Comments
1	30.0	5.0	0.9	July, very humid, "land" surface
2	30.0	20.0	0.9	July, low humidity, "land" surface
3	30.0	5.0	0.7	July, very humid, "ocean" surface
4	30.0	20.0	0.7	July, low humidity, "ocean" surface
5	30.0	15.0	0.9	July, moderate humidity, "land" surface
6	0.0	15.0	0.9	January, low humidity, "land" surface
7	30.0	15.0	0.7	July, moderate humidity, "ocean" surface
8	0.0	15.0	0.7	January, low humidity, "ocean" surface

the radiometric temperature contrast between emission from the warm lower troposphere and the surface contribution. That is, the change in atmospheric emission from the moist to the dry sounding becomes greater in proportion to the surface signal when surface emissivity is low. This increased T_B sensitivity to water vapor over the ocean is consistent with Kakar and Lambrigtsen (1984), Isaacs and Deblonde (1987), and Wilheit (1990), who found that lower-tropospheric water vapor profiles from MW sounders with both water vapor and window channels will be significantly less accurate over land surfaces than the ocean.

Channel 157 represents a transition between window and water vapor channels. Thus, in a very humid atmosphere (soundings 1 and 3 of Table 1) it behaves more like a water vapor channel, with its CF peaking at 860 mb for both "land" ($\epsilon_S = 0.9$) and "oceanic" ($\epsilon_S = 0.7$) surface emissivities. For the drier profile (soundings 2 and 4), channel 157 responds more like the window channels, with its CF peaking at the surface and its surface contributions exceeding 50% for both emissivities. Channels 176–182 show little or no impact from these emissivity changes.

Combining the effects on T_B of temperature changes with those produced by water vapor variations complicates T_B interpretation. Sounding 5 represents a midlatitude July profile with a 1000-mb temperature of 30°C, a 15°C tropospheric T_{dd}, and a "land" surface with an emissivity of 0.9. Sounding 6 denotes a January profile with a 1000-mb temperature of 0.0°C, a 15°C tropospheric T_{dd}, and surface emissivity of 0.9. Although these two profiles represent distinctly different clear atmosphere cases, their T_B's at 182 GHz differ by less than 2 K. Conversely, there is a 40-K difference at 157 GHz. The decrease in water vapor from profile 5 to 6 would, by itself, cause significant warming in channel 182 by lowering the CF peak from 410 to 730 mb. However, this effect is nearly compensated by the 30°C cooling of the temperature profile. Thus, channel 182 senses the temperature of water vapor in the *upper* troposphere of sounding 5, but senses the temperature of the *lower* tropospheric water vapor in sounding 6, and even receives 5.7% of its T_B contribution from the surface. Wang et al. (1992) recently exploited the relative transparency of dry northern latitude atmospheres to calculate precipitable water from aircraft measurements near 183 GHz. Channel 176 is sensitive to conditions nearer the surface, receiving only a 1.8% surface contribution with sounding 5, but 60.1% from the surface for sounding 6. Only CFs for channels 180 and 182 do not peak at the surface for cold, dry sounding 6.

Again, surface emissivity exerts a profound influence on T_B's from the lower-frequency AMSU moisture channels. Soundings 7 and 8 are identical to soundings 5 and 6 (Table 2), but use an "oceanic" surface emissivity of 0.7. The T_B spread between soundings 7 and 8 (Table 1) for channels 1–5 is greater than that from soundings 5 and 6 because the drier sounding allows much more of the surface contribution to come through. The T_B spread for channel 182 is approximately the same as before. This suggests that surface effects might be separated from atmospheric effects by comparing the variability of T_B's from surface sensitive channels to those of water vapor sensitive channels, or even oxygen channels from AMSU-A.

b. *Effects of liquid clouds*

1) CLOUD LIQUID WATER VERSUS CLOUD WATER VAPOR

Section 4b examines how various properties of liquid water clouds affect TOA T_B's. We begin by separating T_B effects due to cloud water from those strictly due to the presence of the saturated layer within the cloud. Our procedure is to first superimpose a saturated layer (Fig. 1d, dashed) and then altostratus cloud on the original uniform dewpoint profile of Fig. 1d (solid). Figure 1b shows CFs when the saturated layer (0°C T_{dd}, but no cloud water) is added between 5 and 6 km (570–490 mb). The CFs for all channels gain a primary or secondary peak within the moist layer. The greatest T_B change occurs in channel 180, from 265 K with no moist layer to 261 K. Conversely, channel 182 shows little change because a substantial portion of its radiance emanates from above the 5–6-km layer.

For the temperate, midlatitude land ($\epsilon_S = 0.9$) conditions used here, the saturated layer produces char-

acteristically distinct T_B changes at 23.8 GHz (Figs. 1a and 1b) compared with frequencies at or above 157 GHz. Specifically, while the layer attenuates T_B's near 157 and 183 GHz by absorbing and reemitting the radiation from below at cooler temperatures, T_B's for channel 23.8 increase slightly (from 275.62 to 275.86 K). Since the temperature of the humid layer ranges from approximately 268 K at its bottom to 260 K at the top (i.e., cooler than the radiometric surface background temperature of 268 K), emission alone cannot explain the warmer T_B. However, examining the different components of TOA T_B's described by the CF formulation (section 2) does provide an explanation and reveals the balance of attenuating and emitting processes that can lead to warmer *or* cooler T_B's by adding a moist layer. Liu and Curry (1993) have addressed how MW T_B's change with increasing optical depth. Below 5 km, atmospheric contributions [given by (4)] are slightly smaller for the profile containing the saturated layer than for the drier profile. While the radiative sources for these layers do not change between the different profiles, the optical depth τ between them and the satellite does become slightly greater with the addition of the absorbing medium (the moist layer), thereby decreasing the transmittance $\exp(-\tau/\mu)$. Since the transmittance above 6 km is virtually the same for both profiles, the greater optical depth $\delta\tau$ of the saturated layer between 5 and 6 km contributes more upwelling radiance than does the uniform profile for the same layer. Above 6 km, atmospheric contributions from corresponding layers are essentially equivalent. Thus, in terms of upwelling atmospheric contributions, the moist layer adds radiance, but also attenuates radiance emanating from below by an even greater amount. By themselves, these processes would lead to cooler T_B's in the presence of a saturated layer.

Therefore, it is the surface boundary contribution (6) that leads to the warmer TOA T_B for channel 23.8. Specifically, since surface emission $\epsilon_S T_S$ is constant for the two profiles (Fig. 1d), only the surface reflection term can account for the warmer T_B. In fact, before attenuation, 6.13 K of radiance reflects from the surface of the moister profile compared with 5.68 K from the uniform T_{dd} profile. After attenuation by the entire atmosphere, surface reflection contributes 5.36 K versus 5.03 K, respectively. Thus, it appears that the additional downwelling radiation emitted from the saturated layer and then reflected back upward and transmitted to the satellite supplies just enough radiance to compensate for the increased attenuation by that moist layer. The phenomenon of T_B's warming with the addition of a moist or cloudy layer above a cool radiometric background is well known for MW window channels. The consequence for image interpretation of the case presented here, however, is that the addition of water vapor to a layer cooler than the surface radiometric temperature may still slightly warm the T_B's of channels having a large surface contribution. Except under extremely dry conditions, this phenomenon would not be likely in the higher-frequency water vapor absorption channels near 183 GHz.

Clouds exert a major influence on the CFs and T_B's of the AMSU moisture channels. Superimposing an altostratus cloud with LWC of 0.4 g m^{-3} and mode radius of 4.5 μm on the saturated layer between 5 and 6 km (Fig. 1c) depresses T_B's in channels 89–182, but increases the T_B in channel 23.8. As simulated in Isaacs and Deblonde (1987), Muller et al. (1992), and Diak et al. (1992), the cloud water further deforms the contribution (or weighting) functions from their clear-air counterparts (Fig. 1a). Analyzing atmospheric and surface contributions as done above provides a similar explanation for the warming in channel 23.8. Scattering can be neglected because in this case, volume absorption coefficients at 23.8 GHz are six orders of magnitude larger than volume scattering coefficients, and four orders larger at 182.31 GHz. Cloud water has a substantial impact on channels 157 and 176, reducing T_B's by 12 and 8 K, respectively, from those of the saturated layer alone (Figs. 1b and 1c). In going from a sounding with no moist layer to one having a moist layer plus cloud, the T_B's in channels 157 and 176 decrease by 13 and 12 K, respectively (Figs. 1a and 1c). Thus, in channel 157, the moist layer alone accounts for only 7% of the total decrease, while cloud water contributes 93%. However, for channel 176, located on the wings of the 183-GHz water vapor absorption line, the moist layer yields 33% of the depression, while cloud water accounts for 67%. Although the T_B depression from water vapor and clouds is small in channel 182 because of overlying water vapor, the 1.3-K T_B decrease from the saturated layer constitutes 89% of the total decrease (1.46 K) due to both water vapor and cloud water. The important point is that while clouds can have a substantial impact on AMSU moisture channel T_B's, a significant portion of that effect is due to the vapor within the saturated cloud layer.

2) Effects of droplet mode radius and size distribution

We now address an issue that has received little previous attention, that is, MW radiative scattering by droplets smaller than precipitation size. Microwave modelers often have treated cloud water in terms of absorption–emission processes based on liquid water content using the Rayleigh approximation (e.g., Ulaby et al. 1981). Falcone et al. (1979) have shown that this is appropriate for small particle sizes at microwave frequencies (e.g., drop size distributions with mode radii less than 10 μm). However, Fraser et al. (1975) showed that while the Rayleigh approximation at 300 GHz is valid for fair weather cumulus, it is not adequate for cumulus congestus at this frequency. Mugnai and Smith (1988) have indicated that a large droplet mode can cause appreciable MW extinction due to Mie scat-

tering, and Wiscombe et al. (1984) asserted that very large cloud droplets may be more common than previously thought.

To further explore the issue of Mie scattering from large cloud droplets, we have investigated radiative effects from a range of SDFs. SDFs having mode radii increasing in multiples of 10 μm through 100 μm were prepared by adjusting values of the original altostratus distribution used in Fig. 1c. Each SDF then was scaled to yield a constant LWC of 0.41 g m^{-3}, equivalent to the unscaled altostratus drop distribution of Falcone et al. (1979). The resulting SDFs and the original with a mode radius of 4.5 μm are shown in Fig. 2a. These clouds were placed in the 600–500-mb layer for the T_B simulations.

The effect on T_B of increasing the mode radius is seen in Fig. 2b. Channels 157 and 176 are affected significantly at mode radii larger than about 20 μm. Effects on channel 89 are important beyond 30–40 μm. Only absorption/emission is significant for drop sizes in the Rayleigh regime; that is, attenuation is proportional to LWC, which we hold constant. Therefore, the varying T_B's indicate that Mie scattering becomes important for these drop distributions. Changes in mode radius have little impact on channels 180 and 182, only because their effects are muted by absorption/emission from intervening water vapor above cloud top. Channel 23.8 is unaffected by the varying droplet distributions due to its lower frequency.

To fully understand these results, it is necessary to relate scattering and extinction to the entire droplet spectrum for each SDF, and not simply to its mode radius. Therefore, extinction and scattering coefficients for channel 157 were plotted as a function of droplet

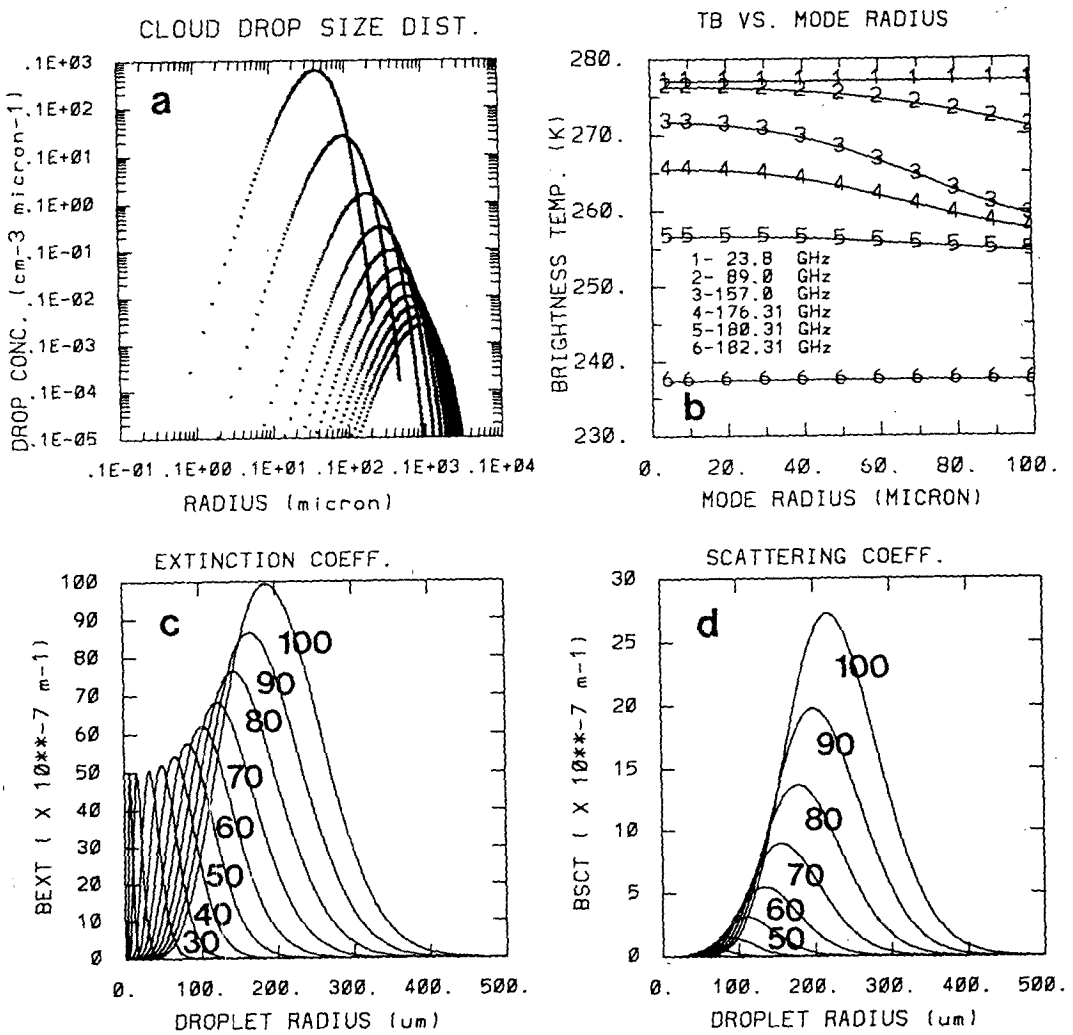

FIG. 2. (a) Droplet number concentration as a function of radius interval (number of droplets per cubic centimeter per micron) for various theoretical cloud droplet SDFs. (b) Brightness temperature T_B as a function of mode radius (μm) of each SDF in (a). (c) Extinction coefficient ($\times 10^{-7}$ m^{-1}) as a function of droplet radius (μm) for each SDF in (a). The mode radius (μm) of the corresponding SDF is given on the right portion of each curve. (d) As in (c) but for scattering coefficient.

radius for each SDF in Fig. 2a (Figs. 2c and 2d). These coefficients are based on a temperature of 268 K (that of supercooled droplets near the middle of the cloud layer) and an LWC of 0.41 g m^{-3}. From left to right, each curve in both panels corresponds to SDFs with progressively larger mode radii. Figures 2a and 2d reveal an important result: though there are fewer large droplets, the greatest scattering for each curve occurs at radii much larger than the mode radius for that particular SDF. For example, the scattering coefficient curve corresponding to a mode radius of 40 μm peaks near 90 μm, while the curve corresponding to a mode radius of 100 μm peaks near 210 μm.

Greatest values of the extinction coefficients (Fig. 2c) are at least four times larger than those of the scattering coefficient (Fig. 2d). Thus, absorption is the dominant extinction process for all the SDFs, but Mie scattering becomes increasingly important for the larger particle sizes. Extinction peaks occur at somewhat smaller radii than for scattering but still are associated with the large droplet tails. For example, the peak extinction for a 60-μm mode radius SDF occurs near 100 μm. Summarizing these results, Mie scattering becomes important beyond a mode radius of 20 μm at 157 and 183 GHz, and beyond 30–40 μm at 89 GHz, due mainly to droplets larger than the mode radius in the tail of the distributions. Rauber (1992) presented a droplet spectrum for an orographic cloud with mode radius of 30 μm, and Pruppacher (1981) quoted several studies showing mode radii between 30 and 40 μm for tropical cumulus and orographic clouds. We have not found examples in the literature of droplet spectra with mode radii larger than 30–40 μm. Nevertheless, for millimeter sounding channels and droplet distributions in the 30–40-μm mode radius range, current results suggest that it may be important to go beyond the Rayleigh approximation, including Mie scattering in the radiative calculations, to deal with the large droplet portions of the SDFs. This may be especially important for possible future MW instruments at frequencies even higher than 183 GHz.

3) Cloud liquid water content, altitude, and thickness

Cloud water content also is an important variable affecting TOA T_B's in the AMSU moisture channels. Figure 3 relates T_B's to cloud water content expressed in terms of liquid water path (LWP). These LWPs range from 0.0 to 0.625 kg m^{-2} for altostratus clouds that are 1 km thick. Again, channels 23.8, 89, 157, 176, 180, and 182 are denoted on the diagram by numbers 1–6, respectively. Figure 3a is for supercooled clouds between 6 and 7 km in altitude (490–410 mb), while results for similar clouds between 2 and 3 km (820–690 mb) are given in Fig. 3b. The LWPs correspond to LWCs ranging from 0.0 g m^{-3} (i.e., a saturated layer, but no cloud water) to 0.50 g m^{-3} in increments

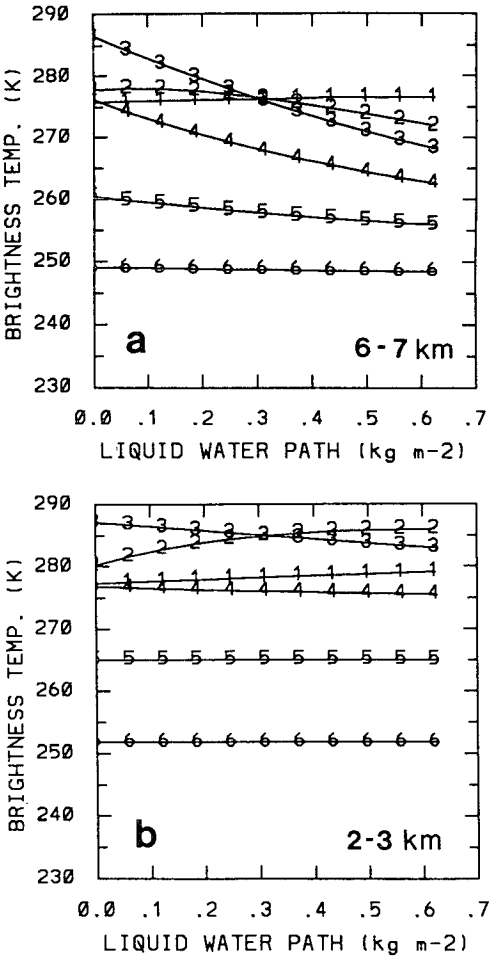

FIG. 3. Plot of T_B (K) as a function of liquid water path (kg m^{-2}) for altostratus clouds between (a) 6 and 7 km and (b) 2 and 3 km in altitude. The T_B curves are labeled 1–6 corresponding to channels 23.8, 89, 157, 176, 180, and 182, respectively.

of 0.05 g m^{-3}. The clouds are superimposed on a sounding with a 1000-mb temperature of 25°C and tropospheric background T_{dd} of 15°C (except for the cloudy layer).

The T_B's for all channels are greater for the warmer 2–3-km cloud (Fig. 3b) than for the colder 6–7-km cloud (Fig. 3a). In addition, T_B's for channels 157–182 of the 6–7-km case are affected more strongly by changes in LWP, generally decreasing with increasing LWP. For example, the channel 176 T_B for the 6–7-km cloud with an LWP of 0.062 kg m^{-2} (0.5 g m^{-3}) is 274 K. This value decreases to 263 K for an LWP of 0.625 kg m^{-2} (0.5 g m^{-3}). For a 2–3-km cloud, the channel 176 T_B at 0.062 kg m^{-2} is 276.5 K, but decreases only slightly to 275.5 K at 0.625 kg m^{-2}. Thus, T_B variability due to variations in water content is enhanced by cloud altitude.

Contribution functions clarify why cloud water variations at higher altitudes have a greater impact on

channels 157–182 T_B's than do variations at lower altitudes. Figure 4 shows CFs for clouds between 6 and 7 km (490–410 mb, Figs. 4a and 4b) and 2 and 3 km (820–690 mb, Figs. 4c and 4d), with LWPs of 0.062 and 0.625 kg m^{-2}. For channels 176, 180, and especially 182, much of the T_B contribution emanates from water vapor above the 2–3-km cloud (i.e., above 690 mb) and thus is affected little by the cloud water content. With channel 182, virtually all of the T_B contribution is from the atmosphere above the 2–3-km cloud, that is, the cloud is virtually obscured by the intervening water vapor. In addition, for channels 157 and 176, the higher, colder cloud provides greater radiometric contrast with the low-level water vapor contributions and warm surface background. This results in greater T_B changes from increasing cloud LWP at high altitude. Recall that the contribution curves are normalized; that is, the integrated area under the CF curves plus the fractional surface contribution equals 1.0. It is clear from Figs. 4a and 4b that increasing the LWC of the higher cloud suppresses T_B contributions from below; that is, the cloud partially obscures the lower atmosphere. For example, at 0.062 kg m^{-2} (Fig. 4a), the channel 176 CF for the higher cloud contains two peaks: a value of 0.2 km^{-1} within the cloud, and the value 0.17 km^{-1} at its "natural" peak near 800 mb, well below cloud height. When LWP is increased to 0.625 kg m^{-2} (Fig. 4b), the channel 176 CF peak within

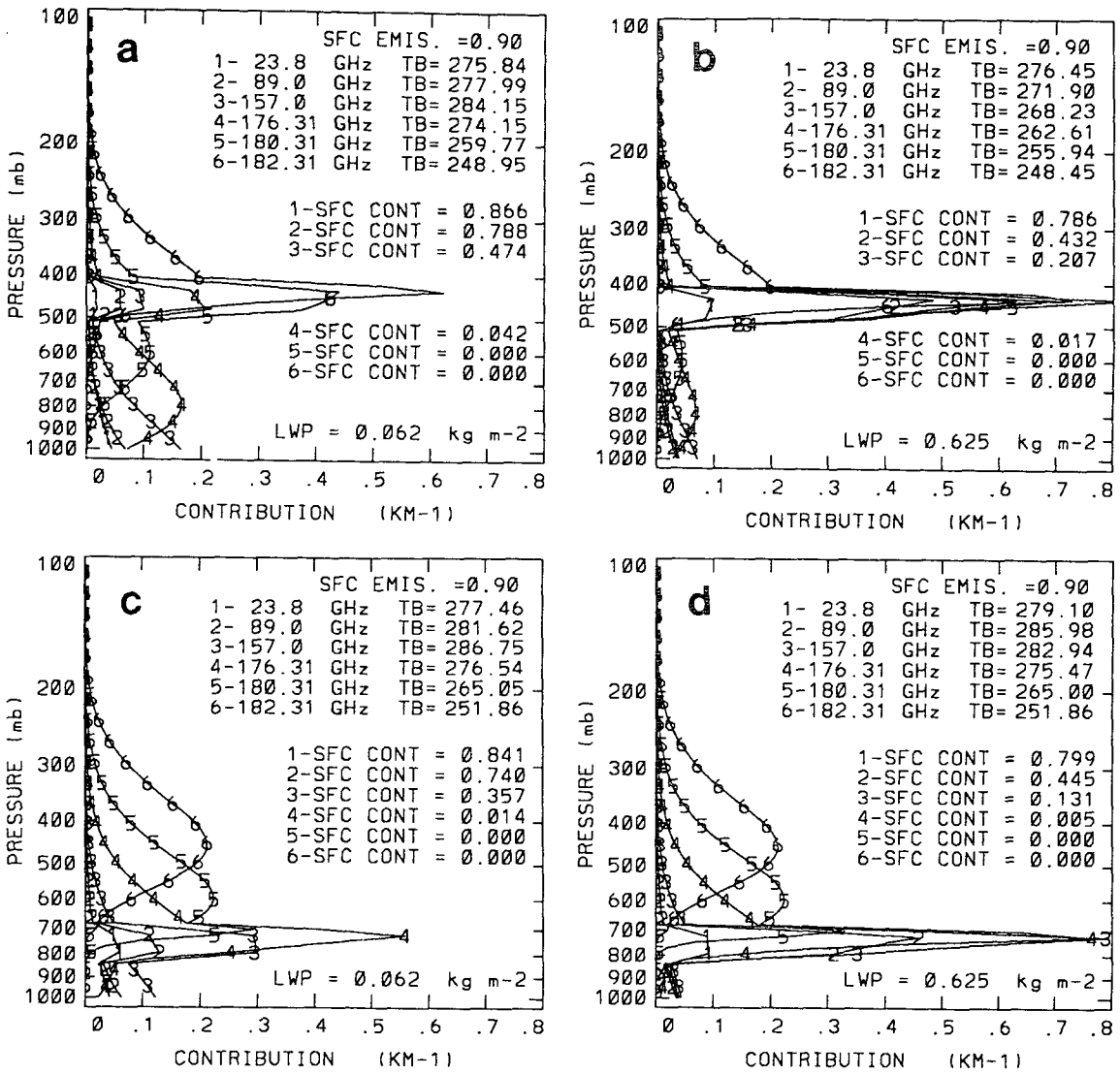

FIG. 4. Contribution functions (km^{-1}) for six AMSU moisture channels for altostratus clouds between (a) 6 and 7 km (490–410 mb) with LWP of 0.062 kg m^{-2}; (b) 6 and 7 km (490–410 mb) with LWP of 0.625 kg m^{-2}; (c) 2 and 3 km (820–690 mb) with LWP of 0.062 kg m^{-2}; and (d) 2 and 3 km (820–690 mb) with LWP of 0.625 kg m^{-2}. The T_B's and fractional surface contributions for each channel are given on the right portion of each panel. Labels 1–6 correspond to channels 23.8, 89, 157, 176, 180, and 182, respectively.

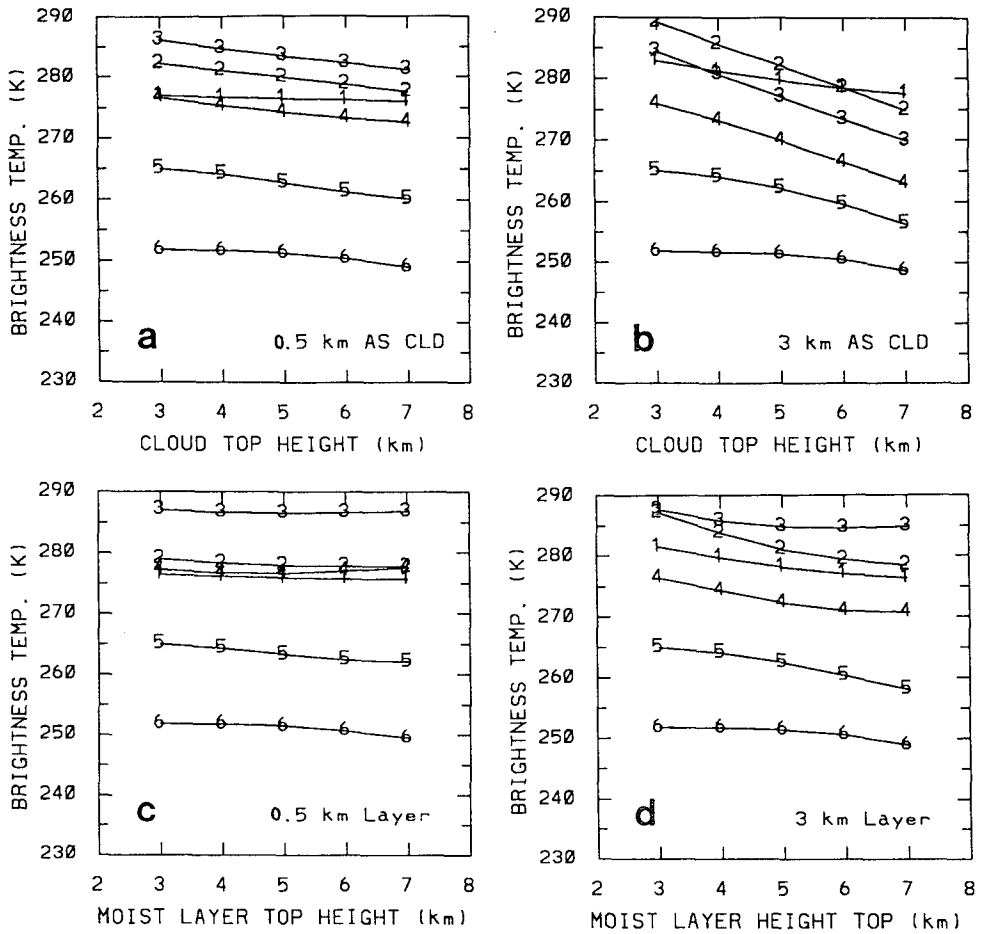

FIG. 5. Plot of T_B (K) as a function of (a) cloud-top height (km) for a 0.5-km-thick altostratus cloud; (b) as in (a) for a 3-km-thick cloud; (c) moist layer top height (km) for a 0.5-km-thick clear but saturated layer; and (d) as in (c) but for a 3-km-thick layer. The T_B curves are labeled 1–6 corresponding to channels 23.8, 89, 157, 176, 180, and 182, respectively.

the cloud increases to a value of 0.7 km^{-1}, while the 800-mb peak decreases to approximately 0.07 km^{-1}, with significantly less area under the lower part of the curve than for the drier cloud.

The T_B's for channels 23.8 and 89 respond differently to increasing cloud water (Fig. 3) than do the higher-frequency moisture channels. Channel 23.8 T_B's for both the low- and high-cloud cases increase less than 2 K with the addition of more cloud liquid water. For a 2–3-km cloud (Fig. 3b) channel 89 T_B's increase from 282 K at 0.062 kg m^{-2} to 286 K at 0.625 kg m^{-2}, while for the 6–7-km cloud (Fig. 3a) channel 89 T_B's decrease by 6 K. Just as with water vapor in a clear atmosphere, the addition of cloud liquid water to a relatively warm layer of the atmosphere yields radiative emissions that contrast with those of the radiometrically cooler surface background contribution. And as cloud liquid water increases for the lower cloud, peak values of corresponding CFs for channel 89 (Figs. 4c and 4d) increase from 0.12 to 0.46 km^{-1} within the cloud layer, while the surface contribution is suppressed from 74% to 45%.

We next examine further details about how changes in cloud altitude affect T_B's. Figure 5 contains plots of T_B variations as a function of the tops of altostratus clouds with thicknesses of 0.5 km (Fig. 5a) and 3 km (Fig. 5b). Each cloud contains 0.2 g m^{-3} of cloud water corresponding to an LWP of 0.150 kg m^{-2} for the 0.5-km-thick cloud, and 0.650 kg m^{-2} for the 3-km-thick cloud. It should be noted that the LWPs may appear slightly larger than suggested by the LWC and the nominal thickness of the cloud due to vertical averaging for layer quantities in the numerical algorithms.

Moving the top of the 0.5-km cloud upward from 3 to 7 km (Fig. 5a) cools T_B's in all channels, but by relatively small amounts. For example, the channel 23.8 T_B decreases only about 1 K, while those of channels 157–180 decrease by 4–5 K. In contrast, cloud-top temperatures decrease 26 K over this range of heights. Thus, variations in equivalent blackbody temperatures measured by a collocated IR sensor should greatly exceed T_B variations measured by AMSU. Compared to the 0.5-km cloud, T_B's for the 3-km-thick

cloud (Fig. 5b) decrease more steeply with increasing cloud height. For example, channel 23.8 decreases over 5 K while channels 89 and 157 cool nearly 15 K. Channels 176 and 180 decrease approximately 13 and 9 K. The T_B variations in channel 182, the most vapor sensitive frequency, are muted by overlying water vapor for both cloud thicknesses. In comparing effects of 0.5-km- and 3-km-thick clouds, it is interesting that slopes of the T_B curves for channels 23.8 and 89 of the thick clouds change mostly by *warming* at the low end of the altitude curve. This response is different from that of IR window measurements, which would be more closely associated with the cloud-top temperature for both clouds. Slopes of the T_B curves for channels 157–182 are steepened mainly by *cooling* the T_B's at the higher altitude cloud tops.

The effects of varying cloud altitudes (Figs. 5a and 5b) should be compared with those due strictly to water vapor, that is, saturated layers with zero cloud water (Figs. 5c and 5d). Moving the top of a 0.5-km saturated layer from 3 to 7 km (Fig. 5c) yields T_B variations ranging from 0.25 K of warming in channel 157 to approximately 3 K of cooling in channel 180. Cooling occurs in all channels for a 3-km-thick moist layer (Fig. 5d). In general, slopes corresponding to altitude changes of the moist layers are smaller than those due to changes in cloud height. The cloudy case T_B curves for channels with strong surface contributions (23.8 and 89) begin at warmer values than those for clear moist layers. However, in the more absorptive channels (176 through 182), the cloud case T_B's nearly equal their clear counterparts at the lower altitudes, but they then cool even more as the cloud is raised. Thus, cloud water accounts for some, but not all, of the height-related T_B variations. Height variations of saturated layers alone exert a substantial influence on T_B's, and these effects are more pronounced for thicker layers.

Surface emissivity varies much more at MW frequencies than for IR channels. This variability was a major source of error for comparisons of SSM/T-2 and collocated aircraft measurements at 91 GHz (Griffin et al. 1993). Figure 6 shows how changing surface emissivity affects T_B's of the AMSU moisture channels. The three panels represent an atmosphere with a saturated moist layer but zero cloud water (Fig. 6a), a cloud with LWC of 0.1 g m^{-3} (LWP of 0.125 kg m^{-2}, Fig. 6b), and a cloud with LWC of 0.5 g m^{-3} (LWP of 0.625 kg m^{-2}, Fig. 6c). All clouds and moist layers are between 4- and 5-km altitude (630 to 570 mb). Surface emissivity increases in increments of 0.1 from 0.5 to 0.9. Surface emissivities of 0.5–0.7 correspond to those found over the ocean, while 0.9 indicates land. Channels 23.8 and 89 are most strongly affected by surface emissivity variations whereas, consistent with Kakar's (1983) results for clear air, the water vapor absorption channels 176, 180, and 182 are virtually unaffected. For example, T_B's for channel 1 range from 196 K at $\epsilon_S = 0.5$, to 276 K at $\epsilon_S = 0.9$ for the single

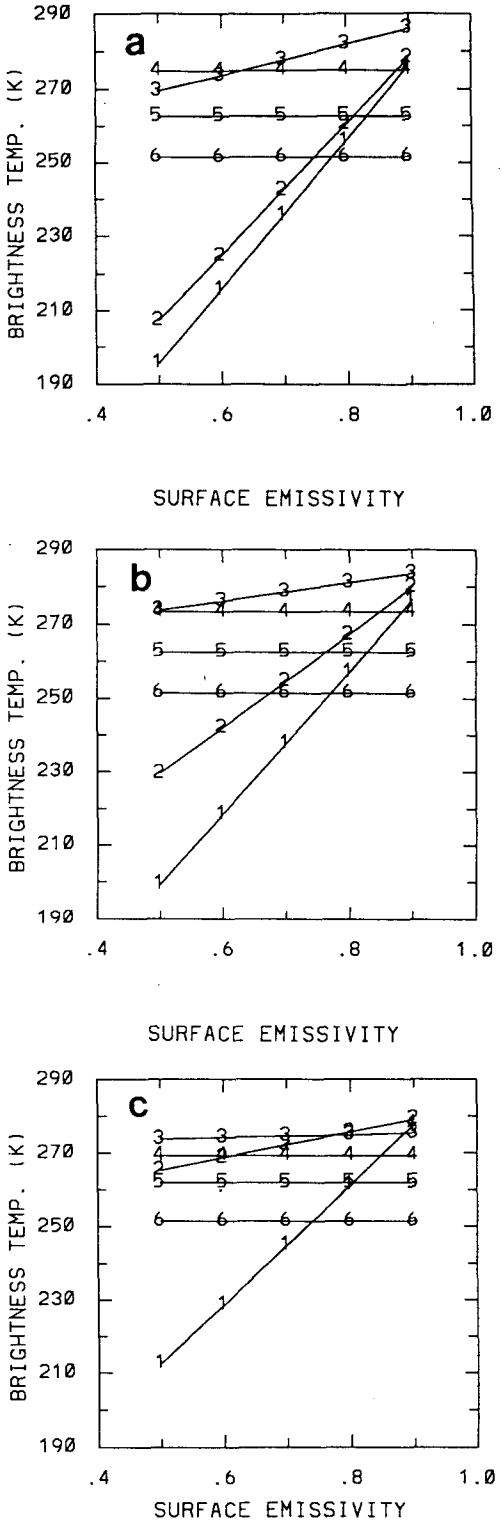

FIG. 6. Plot of T_B (K) as a function of surface emissivity for (a) a clear but saturated moist layer between 4 and 5 km; (b) an altostratus cloud between 4 and 5 km with LWP of 0.125 kg m^{-2}; and (c) as in (b) but with LWP of 0.625 kg m^{-2}. The T_B curves are labeled 1–6 corresponding to channels 23.8, 89, 157, 176, 180, and 182, respectively.

moist layer with no cloud water (Fig. 6a). Adding 0.125 kg m^{-2} of cloud water (Fig. 6b) slightly diminishes the effect of surface emissivity variations in channels 23.8, 89, and 157. Increasing the cloud water content to an LWP of 0.625 kg m^{-2} (Fig. 6c) further diminishes the emissivity effect by obscuring the surface contribution, particularly in channels 89 and 157.

At this point, it is worthwhile to summarize characteristics of AMSU moisture channel T_B's in comparison with IR channel imagery over altostratus liquid clouds. At a relatively small LWP of 0.062 kg m^{-2}, AMSU moisture channels show considerable ability to penetrate clouds (Fig. 4a). This is seen, for example, in significant T_B contributions from subcloud layers of channels 176 and 180. As the LWP increases, the channels' ability to "see" through the clouds diminishes, as indicated by subcloud contributions in Fig. 4b. This sensitivity to LWP has allowed Huang and Diak (1992) to develop AMSU cloud retrieval algorithms from various two-channel combinations. At the same time, the ability to "see" into clouds means that the MW T_B's respond less to variations in cloud altitude than do IR frequencies. Typical altostratus clouds are optically thick (i.e., relatively opaque) in the IR channels so that their equivalent blackbody temperatures correspond more closely to cloud-top temperatures than do the AMSU T_B's. Based on the current research and studies of millimeter-wave signatures over precipitating storms, it appears that AMSU moisture channel imagery will provide information that is intermediate between and complementary to IR frequencies and ground-based weather radars. As is widely recognized, however, special care must be taken in interpreting imagery from surface sensitive MW channels, because surface emissivity variations are much greater at these frequencies than for IR channels.

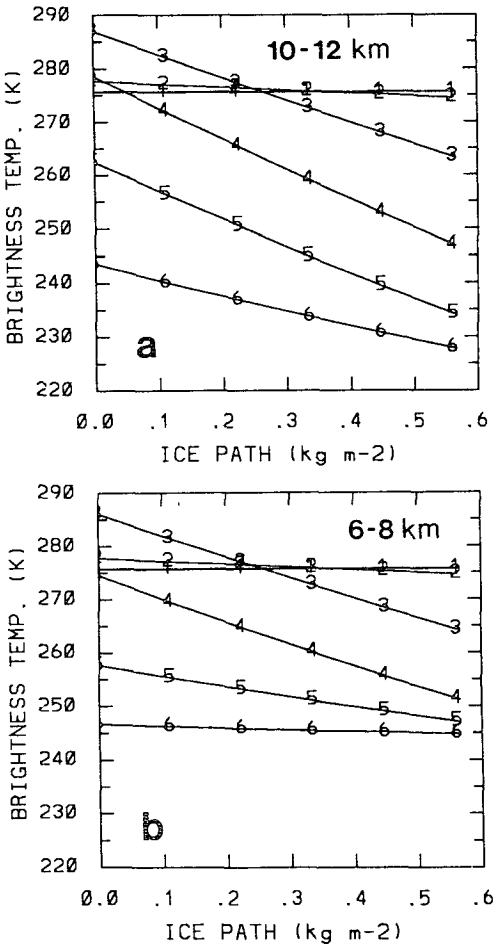

FIG. 7. Plot of T_B (K) as a function of ice water path (kg m^{-2}) for a cirrus cloud between (a) 10 and 12 km; and (b) 6 and 8 km. The T_B curves are labeled 1–6 corresponding to channels 23.8, 89, 157, 176, 180, and 182, respectively.

c. *Effects of ice clouds*

We now examine the effects of cirrus clouds on AMSU moisture channel T_B's. The methodology for these simulations employed the bimodal cirrus uncinus representation described in section 3b. The first issue is the variation of T_B's with cloud ice content. Figure 7 gives T_B's as a function of ice water path (IWP) for 2-km-thick cirrus between 10 and 12 km (300–200 mb, Fig. 7a) and 6 and 8 km (490–360 mb, Fig. 7b). The numbers 1–6 on the diagram refer to channels 23.8, 89, 157, 176, 180, and 182, respectively. The 1000-mb temperature was 25°C, the tropospheric T_{dd} was 15°C (except for 0°C within the cloud layer), and T_d decreased above the tropopause to −80°C, where it became constant. The IWP was varied between 0.0 and 0.563 kg m^{-2} corresponding to IWC increments of 0.05 g m^{-3} from 0.0 to 0.25 g m^{-3}.

Channels 23.8 and 89 are affected little by variations in cirrus ice content at either altitude (Figs. 7a and 7b). At 10–12 km, for example, channel 23.8 T_B's are virtually constant over the entire range of IWPs, while channel 89 T_B's drop only about 3 K. In contrast, cirrus ice content significantly affects channels 157–182, particularly when that ice is at the high altitudes. The T_B's generally decrease with increasing IWP, mainly because of scattering. For example, channel 176 T_B's for a 12-km cloud-top range from 279 K at 0.0 kg m^{-2} IWP to 247 K at 0.563 kg m^{-2} IWP.

Increasing ice contents causes the T_B curves for channels 176, 180, and 182 to converge to cooler values, particularly for the lower cloud (Fig. 7). This results from two effects mentioned in section 2: the channels' differing responses to water vapor versus their comparable responses to ice. Multiple scattering from cirrus particles extracts similar amounts of radiation from channels 176, 180, and 182. However, since there is more water vapor above the 6–8-km cloud than the 10–12-km cloud, the scattering effects of cirrus are more strongly counteracted by water vapor emission above the lower cloud. The result is most prominent

in channel 182, where T_B's for the higher cirrus decrease 16 K as IWP increases from 0.0 to 0.563 kg m^{-2} but decrease only 1.8 K for the lower cloud. The curves of T_B variations with respect to IWP for a 6–8-km cirrus cloud (Fig. 7b) generally are similar in appearance to those with respect to LWP for an altostratus liquid cloud at 6–7 km (Fig. 3a). However, cloud ice appears to produce more attenuation than cloud liquid for equivalent pathlengths at frequencies from 157 to 182 GHz. On the other hand, cirrus ice is more transparent to radiation at 23.8 and 89 GHz than is liquid cloud water.

Contribution functions again explain the response of the various AMSU moisture channels to cirrus clouds. Figure 8 shows CFs for 10–12-km (300–200 mb) clouds at IWPs of 0.113 kg m^{-2} (Fig. 8a) and 0.562 kg m^{-2} (Fig. 8b) and for 6–8-km (490–360 mb) clouds at the same IWPs (Figs. 8c and 8d, respectively). The T_B's for channels 23.8 and 89 receive little contribution from the cloud layers, as observed earlier with their small T_B variations (Fig. 7). The CFs for channel 182 illustrate how the effects of cloud ice and water vapor interact to produce T_B variations. The channel 182 CF for a 12-km cloud top with 0.113 kg m^{-2} IWP (Fig. 8a) has a peak value of 0.21 km^{-1} near cloud top (around 200 mb), and also exhibits a lower but broader peak of 0.11 km^{-1} near 450 mb. Thus, there are substantial T_B contributions from both the cloud layer and the water vapor below. A significant portion of the CF value within the cloud layer is supplied by the water

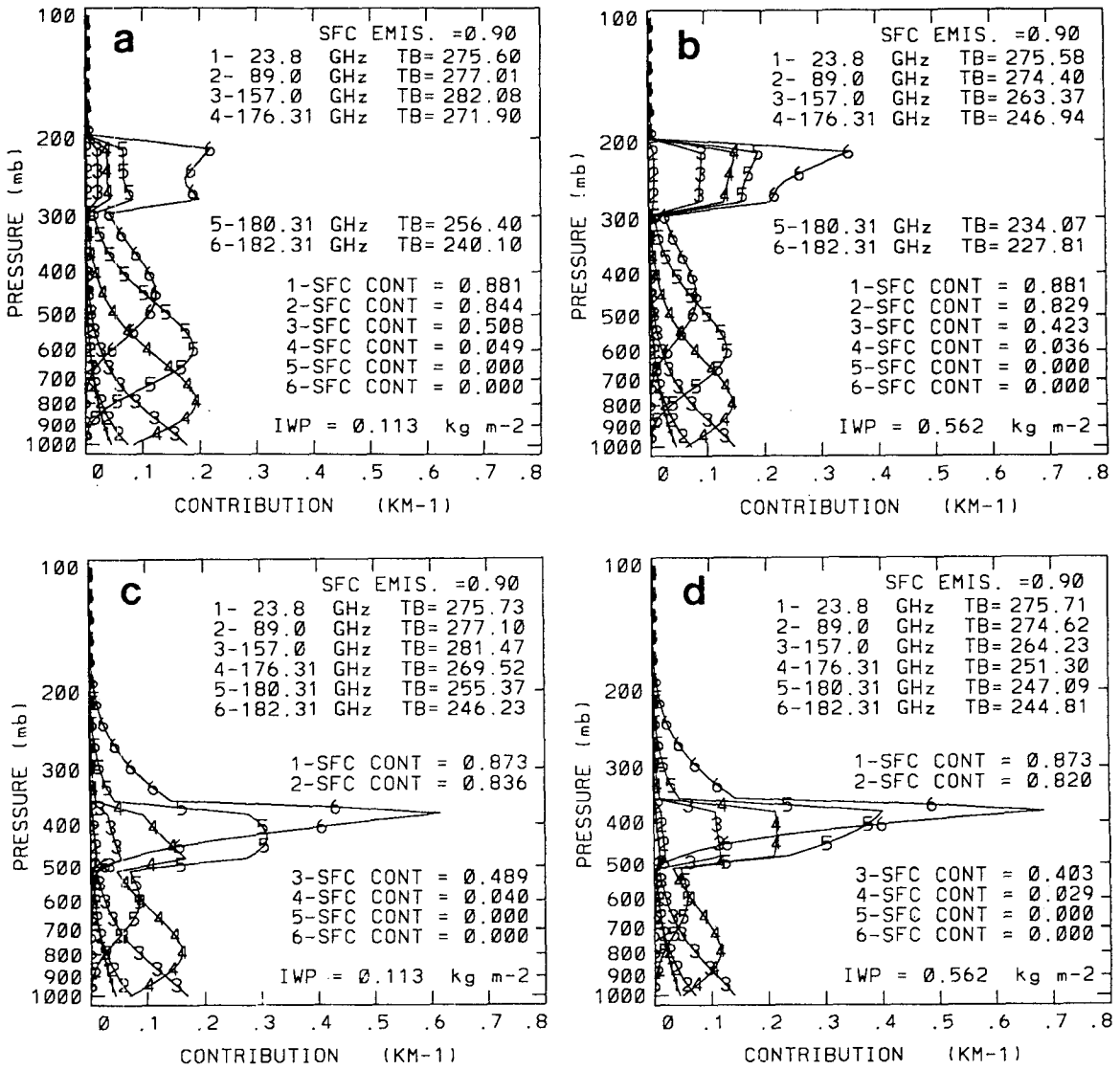

FIG. 8. As in Fig. 4 but for cirrus clouds between (a) 10 and 12 km (300–200 mb) with IWP of 0.113 kg m^{-2}; (b) 10 and 12 km (300–200 mb) with IWP of 0.562 kg m^{-2}; (c) 6 and 8 km (490–360 mb) with IWP of 0.113 kg m^{-2}; and (d) 6 and 8 km (490–360 mb) with IWP of 0.562 kg m^{-2}.

vapor in that layer. Specifically, the channel 182 CF for a moist layer with zero cloud water (not shown) has a peak of 0.19 km^{-1} within the moist layer. For an IWP of 0.562 kg m^{-2} (Fig. 8b), more of the overall T_B contribution emanates from the cloud layer, with the channel 182 CF now peaking at approximately 0.35 km^{-1}. The midtropospheric CF peak decreases to about 0.08 km^{-1}, in conjunction with the T_B cooling seen in Fig. 7a. Attenuation by the cloud of subcloud T_B contributions stems mainly from two processes: absorption by the saturated layer of water vapor and scattering due to the ice particles. This contrasts with altostratus clouds in which the dominant effect of liquid water is absorption of radiation.

For lower cirrus clouds, water vapor constitutes an even greater proportion of the cloud layer's contribution to channel 182 T_B's. The channel 182 CF for a cloud layer between 6 and 8 km (490–360 mb) and IWP = 0.113 kg m^{-2} (Fig. 8c) peaks near 390 mb at 0.62 km^{-1}, while for a moist layer with no cloud ice (not shown) it peaks at 0.60 km^{-1}. When cloud IWP is increased to 0.562 kg m^{-2} (Fig. 8d), the peak CF value increases by only a few percent to 0.68 km^{-1}. Since the cloud is placed near the clear-air CF peak for channel 182, the secondary midtropospheric peak observed for the higher cloud (Fig. 8a) does not occur. This, and the fact that a significant contribution to channel 182 T_B comes from above the cloud, leads to the relatively small T_B changes with IWP for clouds at the 6–8-km level (Fig. 7b).

It is important to examine the effects of cirrus altitude in further detail. Figure 9 shows how T_B's vary with cloud height for 1-km- (Fig. 9a) and 4-km-thick cirrus (Fig. 9b). Abscissas refer to the altitude of the top of the cloudy layers. Again, curves labeled 1–6 correspond to frequencies near 23.8, 89, 157, 176, 180, and 182 GHz. The IWC of each cloud is 0.2 g m^{-3}, corresponding to 0.25 kg m^{-2} and 0.85 kg m^{-2} for 1-km- and 4-km-thick clouds, respectively. Raising a 1-km-thick cirrus layer from 8 to 12 km (Fig. 9a) decreases T_B's for channels 180 and 182 approximately 3 and 8 K, respectively. Channels 23.8–176 are virtually unaffected by these altitude changes.

To understand these T_B variations (Figs. 9a and 9b), one must compare the cloud T_B curves with those produced by a moist layer with no cloud water. Graphs of corresponding T_B changes for 1-km- and 4-km-thick saturated moist layers with zero cloud ice are given in Figs. 9c and 9d, respectively. First, note that T_B's for channels 157–182 generally are cooler with cloud ice (Fig. 9a) than with moist air alone (Fig. 9c). In the case of channels 176 and 180, lifting the top of the clear saturated layer from 8 to 12 km actually warms the T_B's slightly (Fig. 9c). This occurs because the saturated layer between 7 and 8 km contains 1.12 mm of precipitable water, while the one at 11–12 km contains only 0.15 mm. In addition, as the moist layer rises, its cooling effect moves above the range of influence for these channels, thereby allowing more of the warmer, lower-tropospheric T_B contributions to reach the satellite. The channel 176 CF (not shown) for the clear moist layer at 7–8 km has one peak of 0.09 km^{-1}, and a lower-altitude peak of 0.19 km^{-1}. When the saturated layer is between 11 and 12 km, its channel 176 CF peak diminishes to 0.01 km^{-1}, while the lower-level peak increases to 0.21 km^{-1}. Thus, with increasing cirrus height the presence of ice (Fig. 9a) almost exactly counterbalances the effects of saturated layer water vapor changes so that T_B's are nearly constant with increasing cirrus cloud height. In channel 180, the cloud ice actually prevails so that T_B's decrease from 253.1 to 250.2 K over the 4-km range of cloud altitudes. Since ice particles are effective dielectrics, they do not absorb or emit much radiation. Therefore, this cooling is more a result of decreasing emission from the shrinking column of water vapor above the rising cloud than it is of cooling the ice. That is, the scattering signature of the ice becomes more visible as the cloud is raised. In contrast, raising liquid clouds cools T_B's in both the MW and IR spectra by lowering the emitting temperature of the liquid water as well.

Increasing the thickness of the cloudy (Fig. 9b) and moist layers (Fig. 9d) to 4 km accentuates the effects of cloud ice relative to the water vapor for all channels except 23.8 GHz. Differences between channel 23.8 T_B's for cloud ice versus saturation alone are only 0.02–0.03 K. On the other hand, channel 89 T_B's are approximately 5 K cooler for the 4-km-thick cirrus layer than the 4-km clear moist layer. Nevertheless, raising the cloud top from 8 to 12 km yields only a 1.04-K decrease in channel 89 T_B. Multiple scattering from cirrus particles is the only mechanism that can explain the reduction of T_B's by the presence of cloud ice when little change is produced by moving the cloud upward.

The T_B's for channels 180 and 182 (Fig. 9b) provide additional evidence of scattering. Specifically, channel 182 T_B's are warmer than those of channel 180 for cloud tops of 10, 11, and 12 km. For the given atmospheric profile, this can occur only if there is scattering. The dominant effect of scattering is to extract energy out of the radiation's path to the satellite sensor. In channels 176, 180, and 182, energy is added back into the path by emission from water vapor. However, channel 180 is on the wings of the water vapor absorption line. Thus, its T_B's depend more on pressure-broadened line contributions, with less energy emitted back into the path above or within the cloud layer at 180 GHz than at 182 GHz. This effect has been observed over thunderstorms (Heymsfield and Fulton 1988) where high concentrations of ice particles cause T_B's to be much colder than thermometric temperatures of the atmospheric column. The fact that channel 176 T_B's still are warmer than those of either channels 180 or 182 demonstrates that the cirrus has not totally obscured the atmosphere below. Thus, there is a sig-

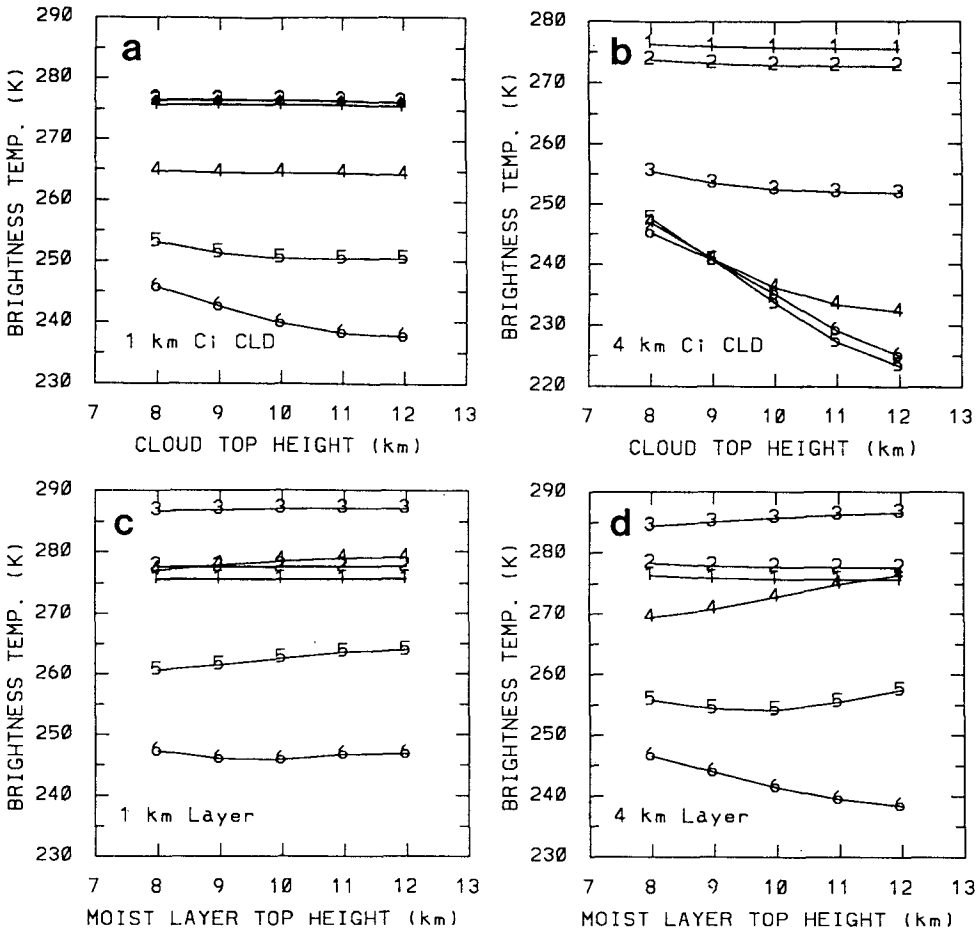

FIG. 9. Plot of T_B (K) as a function of (a) cloud-top height (km) for a 1-km-thick cirrus cloud; (b) as in (a) but for a 4-km-thick cirrus cloud—note difference in temperature scales; (c) moist layer top height (km) for a 1-km-thick clear but saturated layer; and (d) as in (c) for a 4-km-thick layer.

nificant T_B contribution from the lower to middle troposphere at 176 GHz.

It is important to note that unlike IR equivalent blackbody temperatures over optically thick clouds, the calculated MW T_B's often do not match cloud-top temperatures. For example, considering the 4-km-thick cirrus at 12 km (Fig. 9b) where above-cloud water vapor is minimal, T_B's range from 276 K in channel 23.8 to 225 K in channel 182. By comparison, the cloud-top temperature is 229 K. Although not transparent, clouds are penetrable at the AMSU moisture channel frequencies, and the channels "see" through the cloud top to warmer atmospheric layers. On the other hand, scattering can yield T_B's that are much colder than the cloud-top temperature. As a result of both these factors, cloud tops cannot be parameterized as emitting surfaces as is often done in the IR spectrum.

Finally, we consider the effects of surface emissivity in the presence of cirrus clouds. Figure 10 is similar to Fig. 6 for liquid clouds but shows the effects of surface emissivity variations for an atmosphere containing only a saturated layer between 8 and 10 km (Fig. 10a), the same atmospheric profile containing a 2-km-thick cirrus cloud with 0.05 g m^{-3} IWC (0.113 kg m^{-2} IWP, Fig. 10b), and one containing 0.25 g m^{-3} IWC (0.563 kg m^{-2} IWP, Fig. 10c). Consistent with observations at 92 GHz by Hakkarinen and Adler (1988) and Heymsfield and Fulton (1988), T_B's for channels 23.8 and 89 are affected little by the specified amounts of cloud ice, and their T_B's increase rapidly with increasing surface emissivity. Based on the large slopes of these curves, cloud liquid water obscures surface emissivity variations (Fig. 6) in channels 89 and 157 more than does cloud ice (Fig. 10). On the other hand, ice significantly depresses the T_B's for channel 157 at all emissivities, while not changing the slope much from the clear case. As observed with liquid clouds, T_B's of channels 176, 180, and 182 are virtually unaffected by variations in surface emissivity, although the cloud ice does uniformly reduce the T_B's. Thus, channel 157's responses are characteristic of its spectral position between the water vapor absorption channels near 183

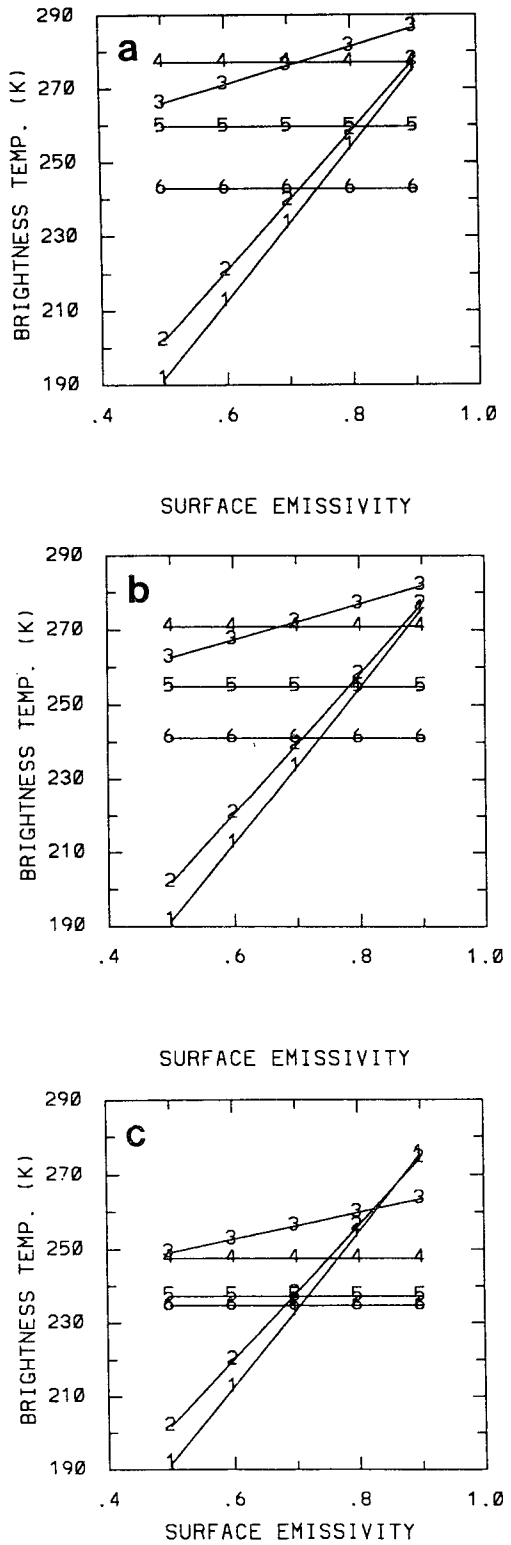

FIG. 10. Plot of T_B (K) as a function of surface emissivity for (a) a clear but saturated layer between 8 and 10 km; (b) a cirrus cloud between 8 and 10 km with IWP of 0.113 kg m^{-2}; and (c) as in (b) but with IWP of 0.563 kg m^{-2}. The T_B curves are labeled 1–6 corresponding to channels 23.8, 89, 157, 176, 180, and 182, respectively.

GHz and the "window" frequency at 89 GHz. That is, like the window channels, its T_B's increase as surface emissivity increases; however, like the higher-frequency water vapor channels, its T_B's are depressed by ice layers.

5. Summary and conclusions

This paper has sought a detailed understanding of atmospheric and surface controls on passive top-of-atmosphere T_B's at moisture sounding frequencies used in the Advanced Microwave Sounding Unit and AMSU-like instruments. Six frequencies were investigated: 23.8, 89.0, 157.0, 176.31, 180.31, and 182.31 GHz. We have performed radiative transfer simulations to document specific examples of how water vapor, along with liquid water and ice particles within nonprecipitating clouds, affect the frequency-dependent T_B's for temperate midlatitude atmospheres, mostly over land. Cloud effects were considered in terms of five basic properties: droplet size distribution, phase, liquid water or ice content, altitude, and thickness. Effects on T_B of changing the surface emissivity also have been addressed. The T_B contribution functions have been presented as an aid to physically interpreting AMSU T_B's.

TOA T_B's for the AMSU moisture channels represent complex interactions between radiation and the earth's atmosphere and surface, including gaseous absorption and emission; absorption, emission, and scattering by cloud and precipitation particles; surface emission; and surface reflection of downwelling radiation. In terms of T_B image interpretation, the AMSU moisture channels can be considered MW analogs to IR window and water vapor channels, but with a number of important differences in their responses to surface characteristics and clouds.

Results of simulations using clear atmospheric profiles provide insight into the effects of temperature and water vapor. Specifically, drying the atmosphere while holding the temperature profile constant was found to move peaks of water vapor channel contribution functions closer to the surface, in agreement with previous investigators. This drying cools T_B's at 23.8 and 89 GHz, but warms values for channels near 183 GHz. Adding the effects on T_B of temperature changes to those produced by water vapor variations complicates T_B interpretation, and various channels were observed to respond quite differently to varying sounding conditions. For example, changing from a moderately dry midlatitude July sounding to a much cooler (and consequently drier) January sounding cooled T_B's at 157 GHz by 40 K, but only 2 K at 182.31 GHz. This small change at 182.31 GHz resulted from the temperature effect (cooling T_B) balancing the drying effect (warming T_B). Surface contributions to T_B are highly dependent on the atmosphere's water vapor content, but generally are large at 23.8 and 89 GHz, and small or nonexistent

near 183 GHz. As noted in previous studies, decreasing the surface emissivity enhances T_B sensitivity to water vapor at 23.8 and 89 GHz.

For temperate midlatitude land conditions, the addition of water vapor or clouds to a clear sounding sometimes yielded results at 23.8 GHz distinct from their effects on the higher-frequency channels. For example, T_B's at 23.8 GHz increased slightly, even when the water vapor and cloud were added to a layer whose thermometric temperature was cooler than the radiometric temperature of the surface background. This resulted from surface reflection of the downward emission from the cloud and moist layer, which then affected upwelling T_B because of additional transmission through the cloud.

The scattering of millimeter-wavelength radiation by liquid droplets smaller than precipitation size has received little previous attention in the literature. Theoretical size distribution functions were examined for their effects on TOA T_B's. Current results indicate that the Rayleigh approximation is adequate for typical cloud drop size distributions. However, Mie scattering effects become important for SDFs with mode radii greater than 20 μm at 157 and 183 GHz, and greater than 30–40 μm at 89 GHz. The scattering results from the relatively small concentrations of droplets much larger than the mode radius. Orographic clouds and tropical cumuli have been observed to contain droplet size distributions with mode radii in the 30–40-μm range. Thus, as new instruments bridge the gap between MW and IR to frequencies higher than those discussed here, radiative transfer modelers are cautioned to explicitly address scattering characteristics of such clouds.

Both liquid and ice clouds were found to impact the T_B's, particularly at higher frequencies. Contribution functions show that clouds depress T_B's of the higher-frequency channels by suppressing or obscuring T_B contributions from below. Liquid water attenuates the upwelling radiance by absorbing and reemitting at a colder temperature, while cirrus ice attenuates through multiple scattering. Clouds affect TOA T_B's near 183 GHz due to both the hydrometeors and the saturated layers of water vapor. The water vapor alone constitutes a significant percentage of the total cloud attenuation.

The T_B's at 23.8 and 89 GHz are more strongly affected by altostratus liquid clouds than by cirrus ice clouds. On the other hand, channels near 157 and 183 GHz are more strongly affected by the ice clouds. This occurs for two major reasons. First, cirrus clouds are higher in the atmosphere, so there is less water vapor above them to obscure the cloud effects. Second, multiple scattering from the ice particles substantially attenuates T_B's at the high frequencies.

Variations in the altitudes of liquid clouds were found to affect T_B's through changes in the cloud's emitting temperature and differences in the water vapor path above the cloud. The altitudes of ice clouds are important at frequencies of 157 and 183 GHz because of the complex balance between the emitting temperature of the water vapor within the cloud, changes in the water vapor content due to lower saturation vapor pressure at higher altitudes, changes in the amount of obscuring water vapor above cloud level, and the scattering effects of the ice particles that depend little on temperature. Thus, with regard to cirrus, the behavior of T_B's at these high frequencies must be explained mainly in terms of multiple scattering from ensembles of ice particles, in conjunction with absorption and emission by water vapor. The water vapor dependence of channels near 183 GHz suggests that a two-channel combination of 183.31 $\pm$ 7.0 and 157 GHz might be even more effective for cloud retrievals than Huang and Diak's (1992) best combination of 183.31 $\pm$ 3.0 and 183.31 $\pm$ 7.0. An ice retrieval scheme such as described by Vivekanandan et al. (1991) could benefit from the high-frequency channels of AMSU, but also should avoid the most water vapor sensitive channels.

For "typical" midlatitude atmospheres, surface emissivity was observed to have a strong impact on T_B's at 23.8 and 89 GHz, but virtually no effect near 183 GHz. Liquid water clouds tend to suppress the effect of surface emissivity on T_B's, particularly at 89 GHz, but nonprecipitating ice clouds are relatively transparent below 89 GHz, and thus do not obscure variations in surface emissivity.

The present results are important for physically interpreting T_B's from new sensors such as AMSU and the SSMIS as well as the recently launched SSM/T-2 moisture sounder. In addition, frequencies *above* 183 GHz show considerable sensitivity to water vapor. Thus, the results presented here have important implications for possible future instruments that might extend to frequencies beyond 183 GHz, both in terms of water vapor effects and scattering from ice and liquid cloud particles. Our future work will employ a mesoscale atmospheric model in conjunction with the radiative transfer model to show how spatial patterns of AMSU water vapor channel imagery can be used to make inferences regarding mid- and upper-tropospheric dynamics and kinematics.

Acknowledgments. We gratefully acknowledge Dr. Eric Smith (FSU) for providing suggestions, computer codes, and reviewing the manuscript. Dr. George Diak (University of Wisconsin—Madison) and Mr. Ralph Ferraro of SM Systems and Research Corporation provided documents related to AMSU. We appreciate the assistance and suggestions of Dr. Pete Robertson of NASA/Marshall Space Flight Center (MSFC). The insightful comments and suggestions of anonymous reviewers helped improve the manuscript. This research has been supported by NASA/MSFC under the Graduate Student Researchers Program Grant NGT-50524.

REFERENCES

Adler, R. F., and I. M. Hakkarinen, 1991: Aircraft multifrequency passive microwave observations of light precipitation over the ocean. *J. Atmos. Oceanic Technol.*, **8,** 201–220.

——, R. A. Mack, N. Prasad, H.-Y. M. Yeh, and I. M. Hakkarinen, 1990: Aircraft observations and simulations of deep convection from 18–183 GHz. Part I: Observations. *J. Atmos. Oceanic Technol.*, **7,** 377–391.

——, H.-Y. M. Yeh, N. Prasad, W.-K. Tao, and J. Simpson, 1991: Microwave simulations of a tropical rainfall system with a three-dimensional cloud model. *J. Appl. Meteor.*, **30,** 924–953.

Boucher, D. J., B. H. Thomas, and A. M. Kishi, 1993: Performance of the DMSP SSM/T-2 microwave radiometer: A comparison between sensor derived, model analyzed, and radiosonde measured moisture variables. Preprints, *Eighth Symp. on Meteorological Observations and Instrumentation,* Anaheim, Amer. Meteor. Soc., J150–J152.

Deirmendjian, D., 1969: *Electromagnetic Scattering on Spherical Polydispersions.* Elsevier, 290 pp.

Diak, G. R., D. Kim, M. S. Whipple, and X. Wu, 1992: Preparing for the AMSU. *Bull. Amer. Meteor. Soc.*, **73,** 1971–1984.

Evans, K. F., and J. Vivekanandan, 1990: Multiparameter radar and microwave radiative transfer modeling of nonspherical atmospheric ice particles. *IEEE Trans. Geosci. Remote Sens.*, **28,** 423–437.

Eyre, J. R., 1990: The information content of data from operational satellite sounding systems: A simulation study. *Quart. J. Roy. Meteor. Soc.*, **116,** 401–434.

Falcone, V. J., L. W. Abreau, and E. P. Shettle, 1979: Atmospheric attenuation of millimeter and submillimeter waves: Models and computer code. Report AFGL-TR-79-0253, Air Force Geophysics Lab., Hanscom Air Force Base, Bedford, MA, 76 pp. [NTIS ADA084485.]

Felde, G. W., and J. D. Pickle, 1994: Microwave earth surface emissivities at 91 and 150 GHz. Preprints, *Eighth Conf. Atmos. Radiation,* Nashville, Amer. Meteor. Soc., 482–484.

Fraser, K. S., N. E. Gaut, E. C. Reifenstein, and H. Sievering, 1975: Interaction mechanisms within the atmosphere. *Manual of Remote Sensing,* Vol. 1, R. G. Reeves, Ed., Amer. Soc. of Photogrammetry, 207–210.

Fulton, R., and G. M. Heymsfield, 1991: Microphysical and radiative characteristics of convective clouds during COHMEX. *J. Appl. Meteor.*, **30,** 98–116.

Griffin, M. K., V. J. Falcone, J. F. Morrissey, R. G. Isaacs, J. D. Pickle, R. Kakar, J. Wang, P. Racette, 1993: The Special Sensor Microwave Water Vapor Sounder (SSM/T-2): Calibration study. Preprints, *Eighth Symp. on Meteorological Observations and Instrumentation,* Anaheim, Amer. Meteor. Soc., J144–J149.

Grody, N. C., 1988: Surface identification using satellite microwave radiometers. *IEEE Trans. Geosci. Remote Sens.*, **26,** 850–859.

Hakkarinen, I. M., and R. F. Adler, 1988: Observations of convective precipitation at 92 and 183 GHz: Aircraft results. *Meteor. Atmos. Phys.*, **38,** 164–182.

Heymsfield, A. J., 1975: Cirrus uncinus generating cells and the evolution of cirriform clouds. Part I: Aircraft observations of the growth of the ice phase. *J. Atmos. Sci.*, **32,** 799–808.

Heymsfield, G. M., and R. Fulton, 1988: Comparison of high-altitude remote aircraft measurements with the radar structure of an Oklahoma thunderstorm: Implications for precipitation estimation from space. *Mon. Wea. Rev.*, **116,** 1157–1174.

Huang, H.-L., and G. R. Diak, 1992: Retrieval of nonprecipitating liquid water cloud parameters from microwave data: A simulation study. *J. Atmos. Oceanic Technol.*, **9,** 354–363.

Isaacs, R. G., and G. Deblonde, 1987: Millimeter wave moisture sounding: The effect of clouds. *Radio Sci.*, **22,** 367–377.

Kakar, R. K., 1983: Retrievals of clear sky moisture profiles using the 183 GHz water vapor line. *J. Climate Appl. Meteor.*, **22,** 1282–1289.

——, and B. H. Lambrigtsen, 1984: A statistical correlation method for the retrieval of atmospheric moisture profiles by microwave radiometry. *J. Climate Appl. Meteor.*, **23,** 1110–1114.

Klein, L. A., and C. T. Swift, 1977: An improved model for the dielectric constant of sea water at microwave frequencies. *IEEE Trans. Antennas Propag.*, **AP-25,** 104–111.

Liebe, H. J., 1985: An updated model for millimeter wave propagation in moist air. *Radio Sci.*, **20,** 1069–1089.

Liu, G., and J. A. Curry, 1993: Determination of characteristic features of cloud liquid water from satellite microwave measurements. *J. Geophys. Res.*, **98,** 5069–5092.

Mugnai, A., and E. A. Smith, 1984: Passive microwave radiation transfer in an evolving cloud medium. *Current Problems in Atmospheric Radiation, Proc. Int. Radiation Symposium,* G. Fiocco, Ed., Hampton, VA, A. Deepak Publishing, 297–300.

——, and —— 1988: Radiative transfer to space through a precipitating cloud at microwave frequencies. Part I: Model description. *J. Appl. Meteor.*, **27,** 1055–1073.

——, H. J. Cooper, E. A. Smith, and G. J. Tripoli, 1990: Simulation of microwave brightness temperatures of an evolving hailstorm at SSM/I frequencies. *Bull. Amer. Meteor. Soc.*, **71,** 2–13.

——, E. A. Smith, and G. J. Tripoli, 1993: Foundations for statistical-physical precipitation retrieval from passive microwave satellite measurements. Part II: Emission-source and generalized weighting-function properties of a time-dependent cloud-radiation model. *J. Appl. Meteor.*, **32,** 17–39.

Muller, B. M., and H. E. Fuelberg, 1990: A simulation and diagnostic study of water vapor image dry bands. *Mon. Wea. Rev.*, **118,** 705–722.

——, H. E. Fuelberg, and X. Xiang, 1992: Brightness temperature simulations for the physical interpretation of AMSU moisture channels. Preprints, *Sixth Conf. Satellite Meteorology and Oceanography,* Atlanta, Amer. Meteor. Soc., 438–441.

——, H. E. Fuelberg, and E. A. Smith, 1993: An alternative representation of the ice canopy for calculating microwave brightness temperatures over a thunderstorm. *J. Appl. Meteor.*, **32,** 1006–1013.

Petersen, R. A., L. W. Uccellini, A. Mostek, and D. Keyser, 1984: Delineating mid- and low-level water vapor patterns in preconvective environments using VAS moisture channels. *Mon. Wea. Rev.*, **112,** 2178–2198.

Pruppacher, H. R., 1981: The microstructure of atmospheric clouds and precipitation. *Clouds: Their Formation, Optical Properties, and Effects,* P. V. Hobbs and A. Deepak, Eds., Academic Press, 93–183.

Rauber, R. M., 1992: Microphysical structure and evolution of a central Sierra Nevada orographic cloud system. *J. Appl. Meteor.*, **31,** 3–24.

Ray, P. S., 1972: Broadband complex refractive indices of ice and water. *Appl. Optics,* **11,** 1836–1843.

Rozenkranz, P. W., M. J. Komichak, and D. H. Staelin, 1982: A method for estimation of atmospheric water vapor profiles by microwave radiometry. *J. Appl. Meteor.*, **21,** 1364–1370.

Saunders, R. W., 1993: Note on the Advanced Microwave Sounding Unit. *Bull. Amer. Meteor. Soc.*, **74,** 2211–2212.

Schaerer, G., and T. T. Wilheit, 1979: A passive microwave technique for profiling of atmospheric water vapor. *Radio Sci.*, **14,** 371–375.

Smith, E. A., and A. Mugnai, 1989: Radiative transfer to space through a precipitating cloud at multiple microwave frequencies. Part 3: Influence of large ice particles. *J. Meteor. Soc. Japan,* **67,** 739–754.

——, A. Mugnai, H. J. Cooper, G. J. Tripoli, and X. Xiang, 1992: Foundations for statistical-physical precipitation retrieval from passive microwave satellite measurements. Part I: Brightness-temperature properties of a time-dependent cloud-radiation model. *J. Appl. Meteor.*, **31,** 506–531.

Starr, D. O'C., and S. K. Cox, 1985: Cirrus clouds. Part I: A cirrus cloud model. *J. Atmos. Sci.*, **42,** 2663–2681.

Swadley, S. D., and J. Chandler, 1992: The Defense Meteorological Satellite Program's Special Sensor Microwave Imager/Sounder

(SSMIS): Hardware and retrieval algorithms. Preprints, *Sixth Conf. Satellite Meteorology and Oceanography,* Atlanta, Amer. Meteor. Soc., 438–441.

Tampieri, F., and C. Tomasi, 1976: Size distribution models of fog and cloud droplets in terms of the modified gamma function. *Tellus,* **28,** 333–347.

Uccellini, L. W., K. F. Brill and C. H. Wash, 1985: The Presidents' Day cyclone of 18–19 February 1979: Influence of upstream trough amplification and associated tropopause folding on rapid cyclogenesis. *Mon. Wea. Rev.,* **113,** 962–987.

Ulaby, F. T., R. K. Moore, and A. K. Fung, 1981: *Microwave Remote Sensing: Active and Passive, Volume 1: Microwave Remote Sensing Fundamentals and Radiometry.* Addison-Wesley, 456 pp.

Vivekanandan, J., J. Turk, and V. N. Bringi, 1991: Ice water path estimation and characterization using passive microwave radiometry. *J. Appl. Meteor.,* **30,** 1407–1421.

Wallace, J. M., and P. V. Hobbs, 1977: *Atmospheric Science: An Introductory Survey.* Academic Press, 467 pp.

Wang, J. R., and L. A. Chang, 1990: Retrieval of water vapor profiles from microwave radiometric measurements near 90 and 183 GHz. *J. Appl. Meteor.,* **29,** 1005–1013.

——, J. L. King, T. T. Wilheit, G. Szejwach, L. H. Gesell, R. A. Nieman, D. S. Niver, B. M. Krupp, and J. A. Gagliano, 1983: Profiling atmospheric water vapor by microwave radiometry. *J. Climate Appl. Meteor.,* **22,** 779–788.

——, T. T. Wilheit, and L. A. Chang, 1989: Retrieval of total precipitable water using radiometric measurements near 92 and 183 GHz. *J. Appl. Meteor.,* **28,** 146–154.

——, and W. C. Boncyk, L. R. Dod, and A. K. Sharma, 1992: Retrieval of total precipitable water over high latitude regions using radiometric measurements near 90 and 183 GHz. *J. Appl. Meteor.,* **31,** 1368–1378.

Warren, S. G., 1984: Optical constants of ice from the ultraviolet to the microwave. *Appl. Opt.,* **23,** 1206–1225.

Weinman, J. A., 1988: The effect of cirrus clouds on 118-GHz brightness temperatures. *J. Geophys. Res.,* **93,** 11 059–11 062.

Welch, R. M., S. K. Cox, and J. M. Davis, 1980: *Solar Radiation and Clouds. Meteor. Monogr.,* No. 39, Amer. Meteor. Soc., 96 pp.

Weldon, R. B., and S. J. Holmes, 1991: Water vapor imagery. NOAA Tech. Rep. NESDIS 57, U.S. Dept. of Commerce, Washington DC, 213 pp.

Wilheit, T. T., 1978: A model for the microwave emissivity of the ocean's surface as a function of wind speed. *IEEE Trans. Geosci. Electron.,* **GE-17,** 244–249.

——, 1986: Some comments on passive microwave measurement of rain. *Bull. Amer. Meteor. Soc.,* **10,** 1226–1232.

——, 1990: An algorithm for retrieving water vapor profiles in clear and cloudy atmospheres from 183 GHz radiometric measurements: Simulation studies. *J. Appl. Meteor.,* **29,** 508–515.

——, A. T. C. Chang, J. L. King, E. B. Rodgers, R. A. Nieman, B. M. Krupp, A. S. Milman, J. S. Stratigos, and H. Siddalingaiah, 1982: Microwave radiometric observations near 19.35, 92, and 183 GHz of precipitation in Tropical Storm Cora. *J. Appl. Meteor.,* **21,** 1137–1145.

Wiscombe, W. J., 1980: Improved Mie scattering algorithms. *Appl. Opt.,* **19,** 1505–1509.

——, R. M. Welch, and W. D. Hall, 1984: The effects of very large drops on cloud absorption. Part I: Parcel models. *J. Atmos. Sci.,* **41,** 1336–1355.

Wu, R., and J. A. Weinman, 1984: Microwave radiances from precipitating clouds containing aspherical ice, combined phase, and liquid hydrometeors. *J. Geophys. Res.,* **89,** 7170–7178.

Xiang, X., 1989: The Delta–Sobolev approach for modeling solar spectral irradiance and radiance. Ph.D. dissertation, School of Earth and Atmospheric Sciences, Georgia Institute of Technology, 178 pp. [Available from University Microfilms International, P.O. Box 1764, Ann Arbor, MI 48106.]

Yeh, H.-Y. M., N. Prasad, R. A. Mack, and R. F. Adler, 1990: Aircraft microwave observations and simulations of deep convection from 18 to 183 GHz. Part II: Model results. *J. Atmos. Oceanic Technol.,* **7,** 392–410.